The Journal of Experimental Biology 205, 3177–3206 (2002)
Printed in Great Britain © The Company of Biologists Limited 2002
JEB4290

A kinematic model of swallowing in *Aplysia californica* based on radula/odontophore kinematics and *in vivo* magnetic resonance images

David M. Neustadter[1,4], Richard F. Drushel[2], Patrick E. Crago[1], Benjamin W. Adams[2] and Hillel J. Chiel[1–3,*]

Departments of [1]Biomedical Engineering, [2]Biology and [3]Neurosciences, Case Western Reserve University, Cleveland, OH 44106-7080, USA and *[4]MR Systems Department, G. E. Medical Systems Israel Ltd, Keren Hayesod Street, PO Box 2071, Tirat Carmel 39120, Israel*

*Author for correspondence at address 2 (e-mail: hjc@po.cwru.edu)

Accepted 3 July 2002

Summary

A kinematic model of the buccal mass of *Aplysia californica* during swallowing has been developed that incorporates the kinematics of the odontophore, the muscular structure that underlies the pincer-like grasping structure, the radula. The model is based on real-time magnetic resonance images (MRIs) of the mid-sagittal cross section of the buccal mass during swallowing. Using kinematic relationships derived from isolated odontophores induced to perform feeding-like movements, the model generates predictions about movement of the buccal mass in the medio-lateral dimension during the feeding cycle that are well-matched to corresponding coronal MRIs of the buccal mass during swallowing. The model successfully reproduces changes in the lengths of the intrinsic (I) buccal muscles I2 and I3 measured experimentally. The model predicts changes in the length of the radular opener muscle I7 throughout the swallowing cycle, generates hypotheses about the muscular basis of radular opening prior to the onset of forward rotation during swallowing and suggests possible context-dependent functions for the I7 muscle, the radular stalk and the I5 (ARC) muscle during radular opening and closing.

Movies available on-line

Key words: feeding, behaviour, biomechanics, kinematics, mollusc, muscular hydrostat, Aplysia californica.

Introduction

Molluscs are adapted to a broad range of environmental niches and feed on a wide range of foods with varying biomechanical properties (Brusca and Brusca, 1990). The molluscan feeding apparatus is characterized by a rasping surface (the radula) and an underlying muscular structure (the odontophore) that is often associated with a cartilaginous structure (bolsters or rotellae; Starmühlner, 1956). A variety of different hypotheses have been proposed to account for the function of these structures. For example, investigators have proposed that the radular surface and underlying odontophore might act like a pulley, a block and tackle, a rasp or a conveyer belt (Eales, 1921; Howells, 1942; Smith, 1988). These hypotheses have been based on observations of the parts of the structure visible during portions of the feeding cycle, histological characterizations of the anatomy and stimulation of individual muscles. For example, careful kinematic analysis of radular kinetics during grazing in *Helisoma trivolvis* indicated that the radula slides over the underlying cartilage, which is independently accelerated during each feeding stroke, supporting a moving conveyor belt hypothesis (Smith, 1988).

Analysis of the radula and odontophore within the buccal mass is complicated by the absence of hard skeletal elements and discrete joints that make musculo-skeletal systems tractable to mechanical analysis. Molluscan feeding structures are composed entirely of muscle and cartilage, and muscle acts both to generate forces and to provide skeletal support. Thus, they are examples of a broader class of structures, muscular hydrostats, that are exemplified by tongues, trunks and tentacles (Kier and Smith, 1985). Because these structures have many degrees of freedom and are thus capable of complex and flexible movements, understanding their biomechanical properties is likely to be essential for a deeper understanding of their neural control. Moreover, the great flexibility of these structures allows them to be utilized for multiple different behavioral functions (e.g. the human tongue is used both for feeding and for talking), and thus the neural architectures controlling these devices are also of special interest for understanding the dynamics of multifunctionality.

We have focused on analyzing the biomechanics and neural control of feeding in the marine mollusc *Aplysia californica*. *Aplysia* is a generalist herbivore that feeds on a variety of red, brown and green seaweeds whose shapes, toughness and texture vary significantly (Carefoot, 1967; Howells, 1942;

Pennings, 1990). The feeding behavior of *Aplysia* is under the control of motivational variables (Kupfermann, 1974) and is subject to associative learning (Chiel and Susswein, 1993; Susswein et al., 1986). The neural control of the feeding apparatus in *Aplysia* has been intensively studied. Sensory neurons responsive to chemical or mechanical stimuli that induce consummatory feeding responses have been identified (Miller et al., 1994; Rosen et al., 1979, 1982, 2000a,b), as have motor neurons for the major muscles of the feeding apparatus (Church et al., 1991; Church and Lloyd, 1994; Gardner, 1993). Neural correlates that distinguish ingestion from rejection have been defined (Cropper et al., 1990a; Morton and Chiel, 1993a,b) and have been used to identify interneurons responsible for flexibly shifting the timing and intensity of activation of motor neuronal pools so that ingestive or egestive behavior can be generated under appropriate conditions (Hurwitz et al., 1997; Jing and Weiss, 2001). Interneurons responsive to mechanical load have been shown to cause the switch from biting to swallowing (Evans and Cropper, 1998).

The kinematics of the buccal mass of *Aplysia* have also begun to be clarified. Earlier studies clarified the functional anatomy of the intrinsic muscles (labelled 'I' followed by a number) and extrinsic muscles (labelled 'E' followed by a number; Howells, 1942). In the present paper, Fig. 21 provides a schematic view of the buccal mass musculature, and Fig. 19 provides a schematic view of the muscles of the radula/odontophore proper. A series of kinematic models of the entire buccal mass has been constructed (Drushel et al., 1998, 2002). These models have provided an increasingly accurate view of the inner workings of the buccal mass, but may not have completely captured the three-dimensional shape of the radula/odontophore. A previous attempt to capture the three-dimensional shapes of the radula/odontophore throughout the feeding cycle (Drushel et al., 2002) used two different approaches. In one approach, the radular halves could move relative to one another and to the radular stalk, creating a three-dimensional shape. This model was referred to as a radular-centric model. In the other approach, the mid-sagittal shape of the odontophore was constrained to be identical to that observed in mid-sagittal magnetic resonance images (MRIs), and the remainder of the three-dimensional shape of the odontophore was determined from the volume of the buccal mass and assumptions about its medio-lateral width. This model was referred to as an odontophore-centric model.

If the full three-dimensional shapes of the buccal mass and its constituent muscles could be simultaneously measured in intact, behaving animals, it would be possible to develop a complete kinematic description of the musculature. Since this is not currently technically feasible, we have developed a technique for obtaining high-temporal- and spatial-resolution planar images of feeding in intact animals using magnetic resonance imaging (MRI). In addition, by inducing feeding-like movements in isolated odontophores in response to pharmacological agents (Drushel et al., 1998; Susswein et al., 1996), it was possible to analyze the kinematics of isolated radula/odontophores in order to derive a set of kinematic relationships for its three-dimensional deformations. By extracting parameters from mid-sagittal MRIs of the radula/odontophore in intact, behaving animals and using them as inputs to a kinematic model based on these kinematic relationships, it was possible to reconstruct the three-dimensional shape of the radula/odontophore throughout the feeding cycle. By combining these odontophore model shapes with a kinematic model of the surrounding musculature, we generated a new odontophore-centric three-dimensional kinematic model of the buccal mass. After validating the overall model, we used it to describe the kinematics of buccal muscles and buccal mass components during swallowing, and compared these predictions with actual measurements. The model generated several testable hypotheses about the context-dependent function of components of the buccal mass that have significant implications for its neural control. Portions of this work have appeared in preliminary form (Neustadter et al., 2001).

As adjuncts to the text, we provide digital movies (in QuickTime format) of the MRIs of swallowing in *Aplysia californica* used for the model presented in this paper, movies of the model construction and movies of the model output. The movie entitled '3_15_39highres.mov' shows interleaved sagittal, coronal and axial images of the buccal mass during swallowing from sequence 7732-S3, frames 15–39. The movies entitled 'ModelProcess.mov', 'ModelProcess2.mov', 'ModelProcess3.mov', 'ModelProcess4.mov' and 'ModelProcess5.mov' illustrate the process by which the three-dimensional kinematic model of the odontophore and the buccal mass is constructed, and will clarify the Materials and methods section. The movies entitled '16-39ModelSideView', '16-39ModelTopView.mov' and '16-39ModelFrontView.mov' show side, top and front orthogonal projections of the kinematic model of the buccal mass for sequence 7732-S3, frames 16–39. These movies will clarify the Results section.

Materials and methods

In this section, we describe the techniques that we used (i) to measure the movements of the isolated radula/odontophore to determine kinematic relationships for its three-dimensional deformations, and (ii) to measure the volume of the radula/odontophore, which was essential for constraining its medio-lateral dimension in the model. We then describe (iii) a new kinematic model of the buccal mass, consisting of a radula/odontophore whose shape was determined from MRIs, and the kinematic relationships deduced from isolated radula/odontophores, as well as a model of the surrounding I3 musculature.

Measurements of the kinematics of the radula/odontophore

To create a complete three-dimensional model of the changing shapes of the radula/odontophore during a feeding cycle, we needed to determine kinematic relationships that would allow us to infer the overall shape of the structure from

planar mid-sagittal MRIs of the structure during feeding. We therefore videotaped and analyzed the relationships between three-dimensional anatomical features seen in multiple planar views of isolated, intact radula/odontophores during spontaneous and drug-induced feeding-like movements. *Aplysia californica* Cooper (160–303 g, obtained from Marinus, Long Beach, CA, USA) (*N*=8) were anesthetized by gradually lowering their body temperature to 4°C using a dissecting tray filled with ice and placing them in a freezer for 30 min. For some studies, animals were anesthetized using magnesium chloride (isotonic 333 mmol l^{-1} $MgCl_2$ equal to half their body mass). The buccal mass was dissected out along with the cerebral and buccal ganglia. The buccal mass was then placed in a dish containing artificial seawater (Instant Ocean, Mentor, OH, USA) at room temperature. The dorsal surface of the buccal mass was cut in an antero-posterior direction along the mid-sagittal line back to the dorsal surface of the esophagus. Much of the I1/I3 tissue on either side of the ventral surface of the radula/odontophore was dissected away so that the base of the radula/odontophore was exposed.

Multiple planar views of the radula/odontophore were obtained simultaneously by mounting two mirrors at 45° to the camera axis, providing three perpendicular views of the preparation that were captured in a single video image. The odontophore was mounted below the mirror that provided a top view and to the left of the mirror that provided a front view. The odontophore itself was oriented to provide the video camera with a side view. A light was shone onto the preparation from above, so that the odontophore's widest medio-lateral extent could be determined during movement by examining the line of shadow that it cast. In one preparation, the anterior edge of the radula/odontophore was mounted on a vertical pin using silk sutures so that the radula/odontophore would have a fixed frame of reference (Fig. 1). Digital NTSC video (Canon ZR10, Canon Inc., Jamesburg, NJ, USA; 30 frames s^{-1}) was used to record the movements of the preparation.

Feeding-like movements were obtained in several ways. As the buccal mass recovered from anesthesia, vigorous spontaneous movements were observed. Crystals of carbachol or dopamine hydrochloride (C-4382 or H-8502, respectively; Sigma, St Louis, MO, USA) were placed on the cerebral ganglion, inducing rhythmic movements (Drushel et al., 1998; Susswein et al., 1996).

Kinematic measurements indicated that several features of the radula/odontophore contributed significantly to the distribution of its volume and should therefore be represented in the three-dimensional model. Moreover, the planar views indicated that the positions and dimensions of these features could be deduced from a mid-sagittal slice (see below). In particular, we identified a wedge-shaped structure that appears to be filled with fluid and is anterior to the I6 muscle, which we refer to as the prow of the odontophore (Fig. 1) (see also fig. 6 in Neustadter et al., 2002). We also recognized that the anterior surface of the radula does not curve smoothly, but forms a ridge as a result of the upward protrusion of the I4 muscles (Fig. 1) (see also fig. 6 in Neustadter et al., 2002). We tracked the movements of these features, as well as monitoring the changing position of the shadow, i.e. the line of widest medio-lateral extent, during the feeding-like movements of the radula/odontophore (see Results for

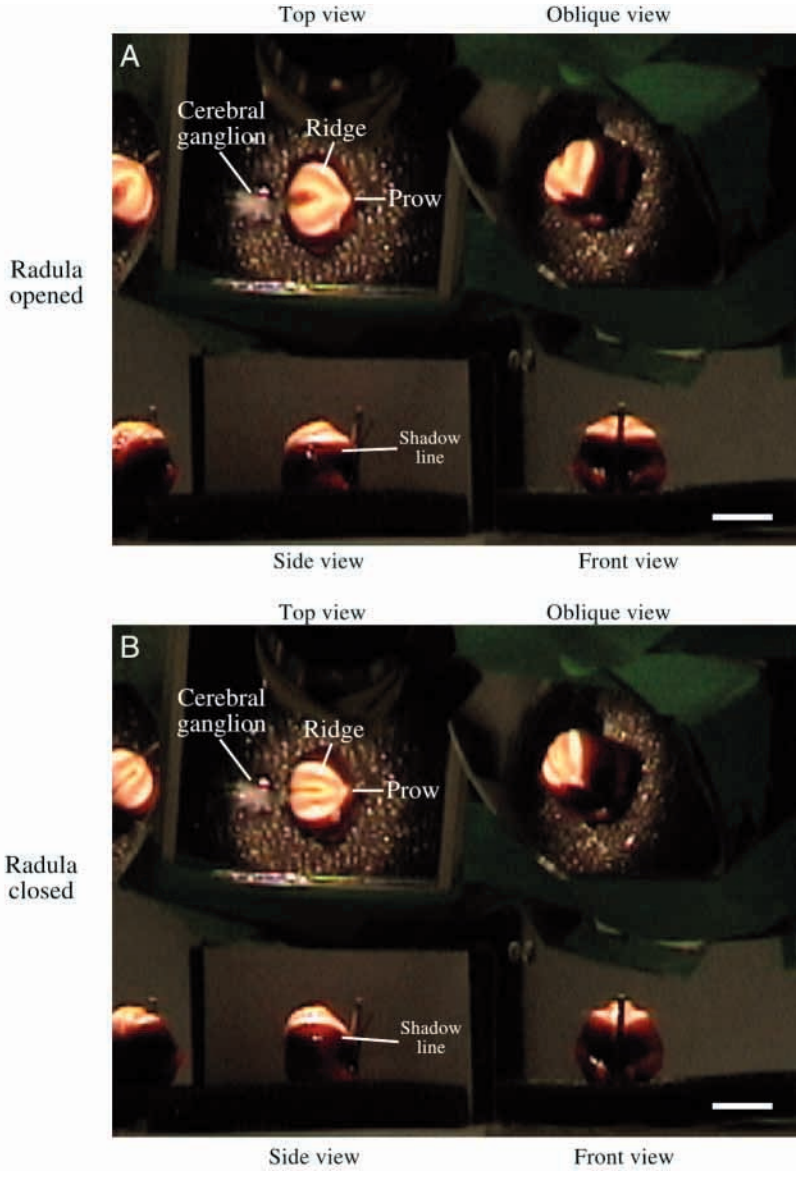

Fig. 1. Measurement of *in vitro* radula/odontophore kinematics. Two frames are shown from a digital video recording of an isolated radula/odontophore induced to perform feeding-like movements in response to carbachol. The line of shadow indicating the region of widest medio-lateral extent is indicated in the side views, and the ridge, prow and cerebral ganglion are indicated in the top views. (A) Multiple views of the open radula and odontophore. (B) Multiple views of the closed radula and odontophore. Scale bars, 10 mm.

measurements and below for a description of how the kinematic relationships were used to deduce rules for the construction of the three-dimensional model of the radula/odontophore).

Measurements of the volume of the radula/odontophore

Given linear measurements from the mid-sagittal plane, and assuming that the radula/odontophore is isovolumetric throughout the feeding cycle, it is possible to use a scaled estimate of the volume to determine the medio-lateral width of the radula/odontophore. We therefore measured the resting volume of the odontophore. The apparatus used to make these measurements consisted of a 60 ml syringe clamped in an upright position and connected *via* a tube to a 0.2 ml glass pipette, which was also clamped in an upright position to approximately the same height. The pipette was used to provide a narrow water column in which small changes in water level could be accurately recorded. Changes in the water level were determined by measuring the height of the meniscus of the fluid in the pipette through a microscope whose eyepiece was equipped with a graduated reticle. To minimize surface tension, which interfered with the free movement of the meniscus, the apparatus was soaked in a solution containing soap (Alconox Detergent Powder; Alconox Inc., New York, NY, USA) for at least 24 h prior to measurements, after which it was rinsed and filled with artificial seawater. The apparatus was calibrated by adding known volumes of water (using an Eppendorf pipette to deliver precise 0.5 ml samples to the apparatus) and recording the changes in the height of the meniscus. The precision of the measurements was ±0.05 ml, and the volumes of the odontophores ranged from 0.4 to 1.5 ml, so that the largest error in measurement of the smallest odontophore was approximately 12%.

As described in previous work (fig. 3 in Neustadter et al., 2002), we have used the internal radular stalk width as a reference length that normalizes lengths and volumes among animals so as to combine measurements from isolated odontophores of different sizes and mid-sagittal MRIs. The volume of the odontophore was therefore normalized to units of (radular stalk width)^3, which we refer to as RSW^3. From measurements performed on five animals ranging in mass from 65 g to 335 g, the mean odontophore volume including the prow and the stalk was computed to be 7.5±0.6 RSW^3 (mean ± S.D., N=5).

Since the prow has a smooth, convex shape, its volume was calculated by reconstructing the three-dimensional volume from three perpendicular projections. The projections were obtained from high-resolution digital photographs, taken through a microscope, of three perpendicular views. The three-dimensional volume was constructed by stacking multiple layers (1 pixel thick) each having the shape of the outline of the prow as seen in the top view. Each layer was scaled in the antero-posterior direction on the basis of the width measured at the appropriate dorso-ventral level in the side view and in the medio-lateral direction on the basis of the width measured at the appropriate dorso-ventral level in the front view. The area of the layers was summed to obtain the volume in cubic pixels and then converted into RSW^3 units. The mean prow volume was computed to be 0.06 RSW^3 or 0.84±0.18% (mean ± S.D., N=4) of the total odontophore volume.

Kinematic model of the buccal mass

The kinematic model consists of the following components: (i) a model of the radula/odontophore, whose three-dimensional shape is based on the kinematic relationships deduced from the studies described above; (ii) a model of the surrounding I3 musculature, based on a modified version of a previous model of these structures (Drushel et al., 1998, 2002); and (iii) an iterative algorithm that positions the radula/odontophore relative to the I3 model muscles so as to best fit the mid-sagittal outline of the buccal mass. We will describe each of these components in turn.

Radula/odontophore model

The three-dimensional shape of the radula/odontophore includes the prow and the radular ridge. The 'radular cleft', i.e. the space between the halves of the radula when it is open, is not included in the model, because it was not possible to identify a measurable parameter on the mid-sagittal MRI that could be used to deduce its medio-lateral and dorso-ventral extents. Potential errors that this introduces in the volume of the radula/odontophore are considered in the Discussion. The model also does not include the narrow ridge that the radular surface forms during and after the peak of retraction (which we refer to as the radular 'pinch'), again because of the absence of a measurable parameter to indicate its extent on the mid-sagittal MRI.

Parameters

Fixed parameters for the model were measured from high-spatial-resolution MRIs of anaesthetized animals and isolated buccal masses, high-spatial-resolution photographs of isolated odontophores and digital video recordings of radula/odontophore kinematics, as described above. The fixed parameters are (i) the overall volume of the odontophore, (ii) the volume of the radular stalk, (iii) the spline parameters describing the vertical and horizontal cross sectional shapes of the odontophore, (iv) the shape of the prow, (v) the volume of the prow and (vi) the parameters defining the shape of the ridge (see Fig. 2; Table 1; see also fig. 3C,D in Neustadter et al., 2002). The spline parameters are used to describe curves using two control points to define a smooth curve between two endpoints (Press et al., 1988) (see legend to Fig. 2).

Parameters for each model frame were measured from mid-sagittal high-temporal-resolution MRIs. The parameters were (i) the outline of the odontophore, including the prow, (ii) the line separating the prow from the odontophore corresponding to the anterior margin of I6, (iii) the point above which to search for the tip of the prow and (iv) the position and orientation of the stalk. The shape of the stalk was based on an outline of the stalk from high-spatial-resolution MRIs and was fixed (see fig. 4 in Neustadter et al., 2002). The stalk outline

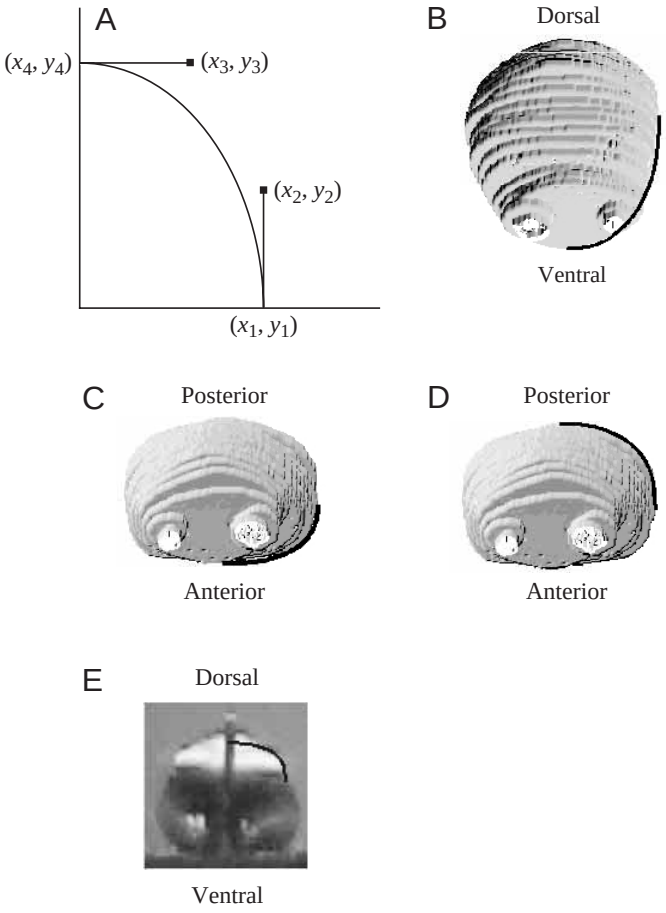

Fig. 2. Extraction of spline parameters from three-dimensional reconstructions based on high-spatial-resolution magnetic resonance imaging (MRI). (A) Definition of spline parameters. The Bezier equations define the x and y positions of the points along the curve with respect to a parameter t, which ranges from 0 to 1 along the length of the curve given the endpoints (x_1,y_1) and (x_4,y_4), and the corresponding control points (x_2,y_2) and (x_3,y_3), which define the curve. In our implementation, the endpoints lie on the perpendicular axes ($y_1=x_4=0$) and the control points are perpendicular to the endpoints ($x_2=x_1$ and $y_3=y_4$), forcing the tangents to the curve at its endpoint to be perpendicular to the axes. As a consequence, the Bezier equations for the curves become $x(t)=(2x_1–3x_3)t^3+3(x_3–x_1)t^2+x_1$ and $y(t)=(3y_2–2y_4)t^3+(3y_4–6y_2)t^2=3y_2t$. The spline parameters given in Table 1 are y_2/y_4 and x_3/x_1, given as fractions to make them independent of scale. When the curve is actually constructed, the two endpoints provide y_4 and x_1; once these endpoints are given, all parameters for the curve are defined. See Table 1 for spline parameter values used in the model that define the lines illustrated in B–E. (B) Extraction of ventral spline parameters. A three-dimensional reconstruction of the odontophore as viewed through the jaws (i.e. with the prow seam vertical) is shown. The spline curve is shown as a dark line at the lower right. Only one side is shown here and in C–E since the structure is bilaterally symmetrical. The white spots at the base of the reconstruction and in the anterior parts of C and D are due to cross sections of the I5 muscle. (C) Extraction of anterior spline parameters. A three-dimensional reconstruction of the odontophore as viewed from its ventral surface (i.e. with the prow seam perpendicular to the plane of the figure) is shown. The spline curve is shown as a dark line at the lower right. (D) Extraction of the posterior spline parameters. Same view as C. The spline curve is shown as a dark line at the upper right. (E) Extraction of dorsal spline parameters excluding the ridge from a video recording of the front view of an isolated odontophore. Since the ridge is not discernible in an anaesthetized buccal mass, these parameters could not be extracted from the high-spatial-resolution MRI data. The spline curve is shown as a dark line at the upper right.

was then scaled for each animal so that it fitted onto the stalk in the image. The following measurements were also made: (v) the outline of the entire buccal mass (including the radular stalk, odontophore and the I3 musculature, but excluding pharyngeal tissue); (vi) the 'lateral groove' (the most posterior part of the I3 musculature); (vii) the 'hinge' (the point of attachment of the ventral radula/odontophore and the most posterior part of the I3 musculature); (viii) the 'line of the jaws' (the location of the most anterior part of the I3 musculature); (ix) an upper limit line that indicated the inner border of the dorsal section of I3; and (x) a lower limit line that indicated the inner border of the ventral section of I3. Extraction of parameters i, ii, iv, v, vi and viii is illustrated in fig. 4 of Neustadter et al. (2002).

Construction of the odontophore

The model creates a three-dimensional mesh that represents the shape of the odontophore. If the odontophore were spherical, one could construct its shape using vertices lying on a number of parallel circles. The diameter of the central circle would be the diameter of the sphere, and the diameters of the other circles would decrease as the circles were further from the center, reaching zero at the front and back of the sphere. To provide an approximately uniform distribution of the vertices on the surface of the sphere, the circles should be spaced in an antero-posterior density corresponding to a cosine function, i.e. more closely spaced at the front and back of the sphere than in the middle.

Because the actual odontophore has a more complex shape, the curves used to define its vertices are not circles but more complex closed convex curves constructed of four spline quadrants. The spline parameters defining the shape of each quadrant are based on projections of radula/odontophores (Fig. 2B,E). The four spline quadrants that compose each curve connect at four anchor points (Fig. 3C). The dorsal and ventral anchor points are defined by the intersection of the plane of the curve with the outline of the odontophore extracted from the mid-sagittal high-temporal-resolution MRIs (Fig. 3A,C). The medio-lateral anchor points are defined by the intersection of the plane of the curve with a curve defining the medio-lateral width (described in the next section; Fig. 3B,C). The spacing between the curves in the antero-posterior direction is cosinusoidal (more closely spaced at the anterior and posterior edges, less closely spaced at the center) to provide approximately uniform coverage of the surface of the odontophore (Fig. 4C).

Table 1. *Fixed parameters of the kinematic model*

Kinematic parameters for the radula/odontophore	
Odontophore volume	7.5 RSW^3
Radular stalk volume	0.69 RSW^3
Prow volume	0.84% of odontophore volume
Spline parameters, dorsal (see Fig. 2E)	0.68, 0.78
Spline parameters, ventral (see Fig. 2B)	0.58, 0.70
Spline parameters, anterior (see Fig. 2C)	0.69, 0.67
Spline parameters, posterior (see Fig. 2D)	0.18, 1.0
Prow parameter s	57.43
Prow parameter x_{max}	95.33
Maximum prow width	0.77 RSW
Arc angle of ridge	100°
Radius of ridge arc	1.23 RSW
Ridge bottom half-width	Odontophore half-width minus 0.46 RSW
Ratio of ridge width top to bottom	0.4
Radius of curvature of ridge trapezoid corner	0.2 RSW
Ridge arc-fitting fraction	0.25
Angle between line of widest extent and line connecting prow tip and top of radula	44±5° (mean ± S.D., N=15)

	Ring number					
	1	2	3	4	5	6
Kinematic parameters for I3 musculature (ring 1 is at the jaws, ring 6 at the lateral groove)						
r	1.248	1.248	1.248	1.3416	1.872	1.7576
a	0.6864	0.4576	0.208	0.5096	0.9776	0.9256
q	0.4472	1.768	4.4096	5.044	4.3472	4.9608
b1	4.2536	3.848	4.212	4.8464	4.3888	4.7528
b2	5.8344	7.1032	8.1224	7.3008	6.136	6.6248

Spline parameters are y_2/y_4 and x_3/x_1 (see Fig. 2 legend) and are given as fractions to make them independent of scale.
RSW, radula stalk width; for details of *a*, *b1*, *b2*, *q* and *r*, see Fig. 6. Values are in arbitrary model units.

Determining the angles of the planes of the closed curves that define the odontophore mesh

The maximum width of each of the closed curves is defined by its intersection with a curve in a plane that cuts through the structure along its widest medio-lateral extent (Fig. 3B). In the previous odontophore-centric model of the radula/odontophore (Drushel et al., 2002), this plane was assumed to be the plane that passed through the anterior and posterior extremes of the mid-sagittal cross section of the odontophore. As a consequence, a series of vertical closed curves could be placed parallel to one another along the line from the anterior extreme to the posterior extreme to include the entire volume of the odontophore (Fig. 4A). Studies of the shadow line on the isolated radula/odontophore during feeding-like movements (see below; see also Fig. 7) demonstrated that the line of widest medio-lateral extent did not necessarily intersect the anterior and posterior extremes of the mid-sagittal cross section of the odontophore. Consequently, if the closed curves were placed parallel to one another and their width was defined by their intersections with the line of widest extent, a portion of the volume of the odontophore would extend past the ends of the line of widest extent and would, therefore, have no defined width (Fig. 4B). To solve this problem, we computed the tangents to the mid-sagittal outline at the posterior and anterior ends of the line of widest extent and set the closed curves at angles that continuously changed from the posterior tangent to the anterior tangent value. This guaranteed that the entire volume was represented by curves that intersected the line of widest extent (Fig. 4C).

Determining the line of widest extent

The position and angle of the line of widest extent were derived using a kinematic relationship based on observations of isolated, moving radula/odontophores. The line of widest extent, which was observed as a shadow line on the moving odontophores, was found to have a fixed angle (44°) relative to the line connecting the top of the radular surface and the tip of the prow and to pass through the tip of the prow (see below; see also Fig. 7). This relationship allowed us to deduce the angle of the line of widest extent, which cannot be directly observed in the mid-sagittal MRIs, from the angle of the line connecting the top of the radular surface and the tip of the prow, which can be directly measured in the MRIs.

To calculate the angle of the line of widest extent in the model, the location of the tip of the prow, the location of the top of the radular surface and the angle of the line connecting

them must be determined. Anatomically, the tip of the prow is the anteriormost end of the radular surface, and there is therefore a large change in curvature at that point along the mid-sagittal outline of the prow (Fig. 3D). To locate the tip of the prow objectively, we therefore implemented an algorithm that identifies the point of sharpest curvature along the top portion of the mid-sagittal outline of the prow. The algorithm selected the point at which the sum of the χ^2 goodness-of-fit errors for linear fits to the portions of the curve above and below the point was minimal. Because the tip and the bottom of the prow were sutured to a vertical pin, this vertical line defined the reference frame in which the top of the radular surface was measured in the moving isolated odontophores. Consequently, before determining the location of the top of the radular surface for the model, the mid-sagittal cross section was rotated so that the line connecting the tip of the prow and the bottom of the prow was vertical (Fig. 3E). After applying this rotation, we identified the topmost point of the mid-sagittal cross section, which was the top of the radular surface. We then defined the line of widest extent to be the line that passed through the tip of the prow and was 44° counterclockwise from the line connecting the top of the radular surface and the tip of the prow (relative to the orientation shown in Fig. 3E).

Construction of the prow

Anatomical studies of the prow indicated that its volume could be treated as constant, that its posterior margin formed a plane with the I6 muscle and that the medio-lateral profile of its anterior edge could be approximated by a Gaussian curve (see Fig. 6C in Neustadter et al., 2002). The Gaussian function used to determine the medio-lateral width x of the prow in terms of its antero-posterior location was:

$$x = \frac{A}{x_{\max}} \sqrt{-2s^2 \log\beta\left[\frac{y}{B}\left(1 - e^{-x_{\max}^2/2s^2}\right) + e^{-x_{\max}^2/2s^2}\right]},$$

in which A and B determine the scaling of the curve in the x and the y dimensions, respectively, and the values of the measured prow parameters s and $x_{\max}$ are given in Table 1.

Two parameters for the prow were extracted from each mid-sagittal MRI: (i) the mid-sagittal anterior margin of the prow and (ii) the line along which it meets I6, which we refer to as the 'prow seam' (see fig. 4B,C in Neustadter et al., 2002; the anterior margin of the odontophore corresponds to the prow seam). The antero-posterior position of the prow seam is later iteratively adjusted to achieve the correct prow volume, but its angle remains unchanged. The entire three-dimensional mesh is constructed in the reference frame in which the prow seam is vertical. To best approximate the actual anatomical shape of the prow (see Fig. 6 in Neustadter et al., 2002), the dorsal half of each curve defining the volume of the prow (i.e. the part of the curve above the line of widest extent) was vertical (i.e. parallel to the prow seam) and the ventral half (i.e. the part of the curve below the line of widest extent) curved posteriorly to meet the other curves at the base of the prow seam (Fig. 3F). The curvature of the ventral half is such that its position is a fixed percentage of the distance between the anterior margin of the prow and the prow seam. The shapes of the dorsal and ventral parts of each curve were defined by the same spline parameters used to define the curves of the rest of the odontophore, and the maximum width at the intersection with the line of widest extent was defined by the Gaussian approximation of the medio-lateral profile of the prow. The width of the Gaussian curve at the prow seam was defined as 0.77 RSW, based on anatomical observations. To achieve the known fixed volume of the prow, the mesh representing the prow was iteratively constructed with the prow seam being moved anteriorly or posteriorly.

Construction of the ridge

Observations of the kinematics of isolated radula/odontophores indicated that it was necessary to include a dorsal ridge. The spline curve used to approximate the shape of the dorsal half of the odontophore does not accurately represent the shape of the dorsal surface throughout the movements of the isolated odontophore (in Fig. 2E, note the discrepancy between the location of the spline curve and the dorsal surface of the odontophore). During a portion of the movement cycle, a ridge projects above this shape. To determine the timing and extent of ridge protrusion during a movement cycle in the isolated radula/odontophore, we used the top view of the radula to locate the posterior and anterior margins of the ridge, and identified these locations in the side view (Fig. 5A). On the basis of empirical measurements, we found that a circular arc (radius 1.23 RSW, arc angle 100°) could be fitted to the dorsal radular surface anterior and posterior to the ridge (Fig. 5B). This arc was therefore fitted to the anterior portion of the odontophore outlines measured on the mid-sagittal MRIs and used to define the ridge for the model. The arc was fitted to 0.25 times the distance between the tip of the prow and the posterior of the odontophore. The arc was continued posteriorly by a straight line tangential to the posterior end of the arc (Fig. 5B), on the basis of empirical observations. A protrusion above this arc indicated the presence of a ridge. If a ridge was observed in the mid-sagittal section of the MRI, we constructed the medio-lateral shape of the ridge (based on empirical observations of the ridge *in vitro*) by constructing a trapezoid whose ventral width was 0.46 RSW less than the maximum width of the odontophore, and whose dorsal width was 0.4 times the ventral width. The radius of curvature of the corner of the trapezoid in the medio-lateral dimension was 0.2 RSW (Fig. 5C, top). For each curve in the region of the protrusion, the dorso-ventral height of the ridge was defined by the height of the protrusion, and the medio-lateral width of the ridge was defined relative to the width of the odontophore at that location. Since the planes of the curves are not necessarily vertical (Fig. 4C), the medio-lateral odontophore width used to determine the ridge width was the maximum of two widths: (i) the width at the intersection of the curve with the line of widest extent or (ii) the maximum odontophore width at the horizontal location of the top of the curve. If the width of the odontophore was less than 1.0 RSW, no ridge was constructed. Otherwise,

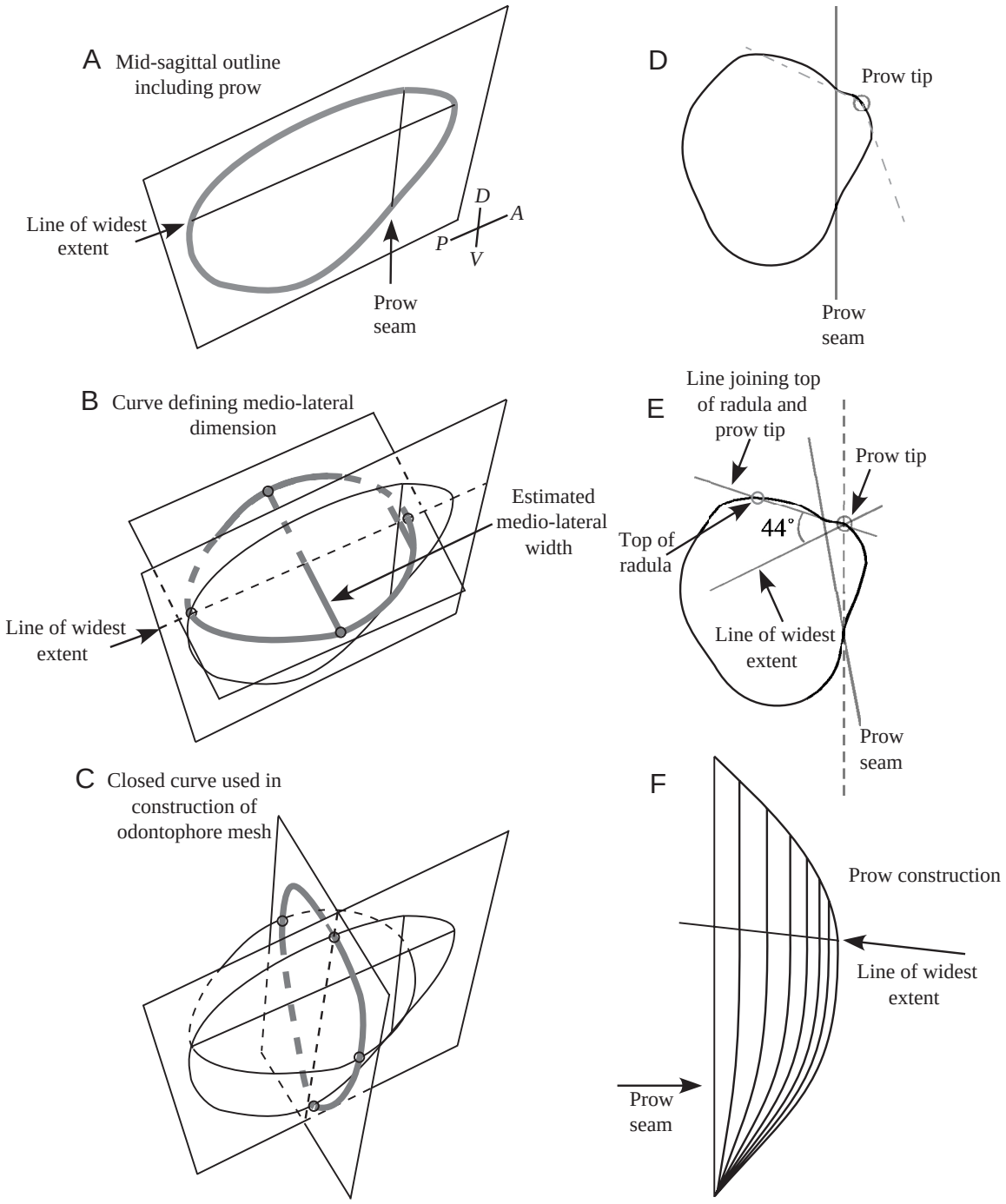

a trapezoid representing the ridge was constructed by relocating the vertices of the curve defining the dorsal edge of the odontophore mesh (Fig. 5C, bottom).

Total volume of the odontophore

Although it was possible to determine the location of the line of widest extent from a mid-sagittal MRI using the kinematic relationships described above, and the shape of the curve in the plane of widest extent was determined by the spline parameters measured from the high-spatial-resolution MRIs of the anesthetized buccal mass, the actual medio-lateral width of the radula/odontophore could not be determined from a mid-sagittal image. Given the assumption that the radula/odontophore is isovolumetric and given the measured volume of the odontophore, the medio-lateral width of the three-dimensional mesh was iteratively adjusted, and the odontophore mesh was reconstructed until the correct volume was achieved. Determining the correct volume required a measure of the volume of the radular stalk and the extent to which it overlapped the volume of the odontophore. The volume of the radular stalk was calculated from a measurement of the radular stalk width and a three-dimensional

Fig. 3. Constructing the odontophore and the prow. (A) Perspective view of a square containing a mid-sagittal outline of the odontophore and prow extracted from high-temporal-resolution magnetic resonance imaging (MRI). The prow seam and the line of widest extent (see D and E and text for definition) are indicated. *A*, anterior; *D*, dorsal; *P*, posterior; *V*, ventral. (B) Curve defining the medio-lateral dimension. The curve lies in the plane that contains the line of widest extent and is perpendicular to the mid-sagittal plane. The curve is constructed of four spline quadrants whose spline parameters are based on high-spatial-resolution MRIs of an anesthetized odontophore (see Fig. 2C,D and Table 1). The four anchor points for this curve at which the spline quadrants meet are defined as follows (each is indicated by a small circle): the posterior anchor point is the intersection of the line of widest extent with the mid-sagittal odontophore outline; the anterior anchor point lies along the line of widest extent, and its position is defined such that the width of the curve at the prow seam is equal to the fixed maximum prow width (see Table 1). The other two anchor points are midway between the prow seam and the posterior anchor point in the antero-posterior direction, and their medio-lateral position is iterated until the correct odontophore volume is achieved. (C) Example of one of the closed curves used in the construction of the odontophore mesh. The antero-posterior intersections of the planes of these curves are illustrated in Fig. 4C. Anchor points are indicated using circles. The dorsal and ventral anchor points are defined by the intersection of the plane of the curve with the mid-sagittal outline of the odontophore (A). The medio-lateral anchor points are defined by the intersection of the plane of the curve with a curve defining the medio-lateral width (B). (D) The tip of the prow is indicated by a grey circle. See Materials and methods for the algorithm that locates it along the anterior margin of the prow. (E) The line of widest extent passes through the tip of the prow. In the orientation shown, its angle is 44° counterclockwise from the line connecting the top of the radular surface and the tip of the prow. The top of the radular surface is defined in the reference frame in which the line connecting the tip of the prow and the bottom of the prow seam is vertical (represented by the vertical dashed line). (F) Construction of the prow. Each line indicated here represents a side view of a closed curve similar to that described in C. The portion of the curve above the line of widest extent is parallel to the prow seam. The portion of the curve below the line of widest extent is bent such that its antero-posterior position remains at the same percentage of the distance between the anterior margin of the prow and the prow seam as it had when it intersected the line of widest extent.

reconstruction of the radular stalk from high-spatial-resolution MRI (see fig. 3C in Neustadter et al., 2002; the value is $0.69\,RSW^3$). The volume of the radular stalk was assumed to be approximately constant, on the basis of the approximately constant area of its cross section in the mid-sagittal MRIs. The position and angle of the radular stalk relative to the odontophore were extracted from the mid-sagittal MRIs. If the radular stalk protruded through the ventral side of the odontophore, as it does during retraction, the protruding portion of the stalk was not included in the outline of the odontophore. To calculate the total volume of the radula/odontophore, it was therefore necessary for the model to calculate the sum of the volumes of the odontophore and the radular stalk and then to subtract the overlapping volume. If the total volume of the odontophore was incorrect, the model iteratively adjusted the medio-lateral width at the line of widest extent and repeated the construction of the three-dimensional odontophore mesh until the volume fell within a pre-defined tolerance ($\pm 0.1\,RSW^3$ of $7.5\,RSW^3$).

Modifications to the kinematic model of the I3 musculature

Once the three-dimensional mesh of the odontophore had been constructed, a model of the I3 musculature was constructed around it based on the previously published kinematic model (Drushel et al., 1998, 2002), which approximates the I3 muscle as a number of distinct rings (Fig. 6A) whose parameters were estimated by trial and error. Because the high-spatial resolution MRIs provided more information about the actual shape of the I3 musculature than had been previously observed, we extracted additional parameters and modified the I3 model so that we could make use of these parameters to produce a better match between the model and the *in vivo* data.

The shape and size of each model I3 ring are defined by five parameters (Fig. 6A): *r*, the radius of the half-circular cross section of the outer half-ring at the top and bottom and of the inner half-ring surrounding the lumen; the thickness of each model ring is 2*r*; *a*, half the maximum width of the lumen; *q*, the width added between the outer and inner half-rings so that the medio-lateral width of the model ring matches the medio-lateral width of the I3 muscle at that location; *b1*, the height of the lumen

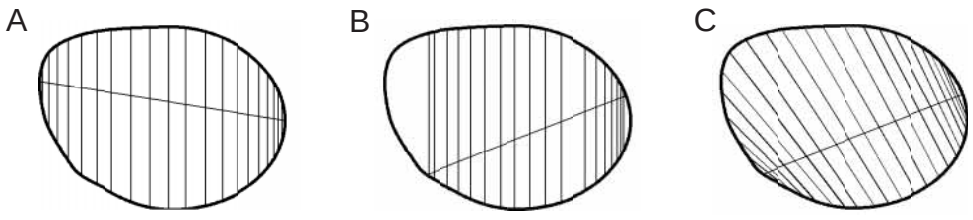

Fig. 4. Selecting curves that define the vertices of the odontophore mesh when the line of widest extent does not pass through the anterior and posterior extremes of the mid-sagittal cross section. In all parts of this figure, note the cosinusoidal spacing of the curves to provide approximately uniform coverage of the odontophore surface. (A) A mid-sagittal shape can be extrapolated into a three-dimensional mesh using vertices that lie along parallel curves and whose widths are defined by their intersection with a line of widest extent, if the line of widest extent passes through the anterior and posterior extremes of the mid-sagittal shape. (B) If the line of widest extent does not pass through the anterior and posterior extremes, then parallel curves whose widths are defined by their intersection with the line of widest extent cannot encompass the entire volume. (C) This problem can be overcome by angling the planes of the curves such that they are tangential to the mid-sagittal shape at both ends of the line of widest extent.

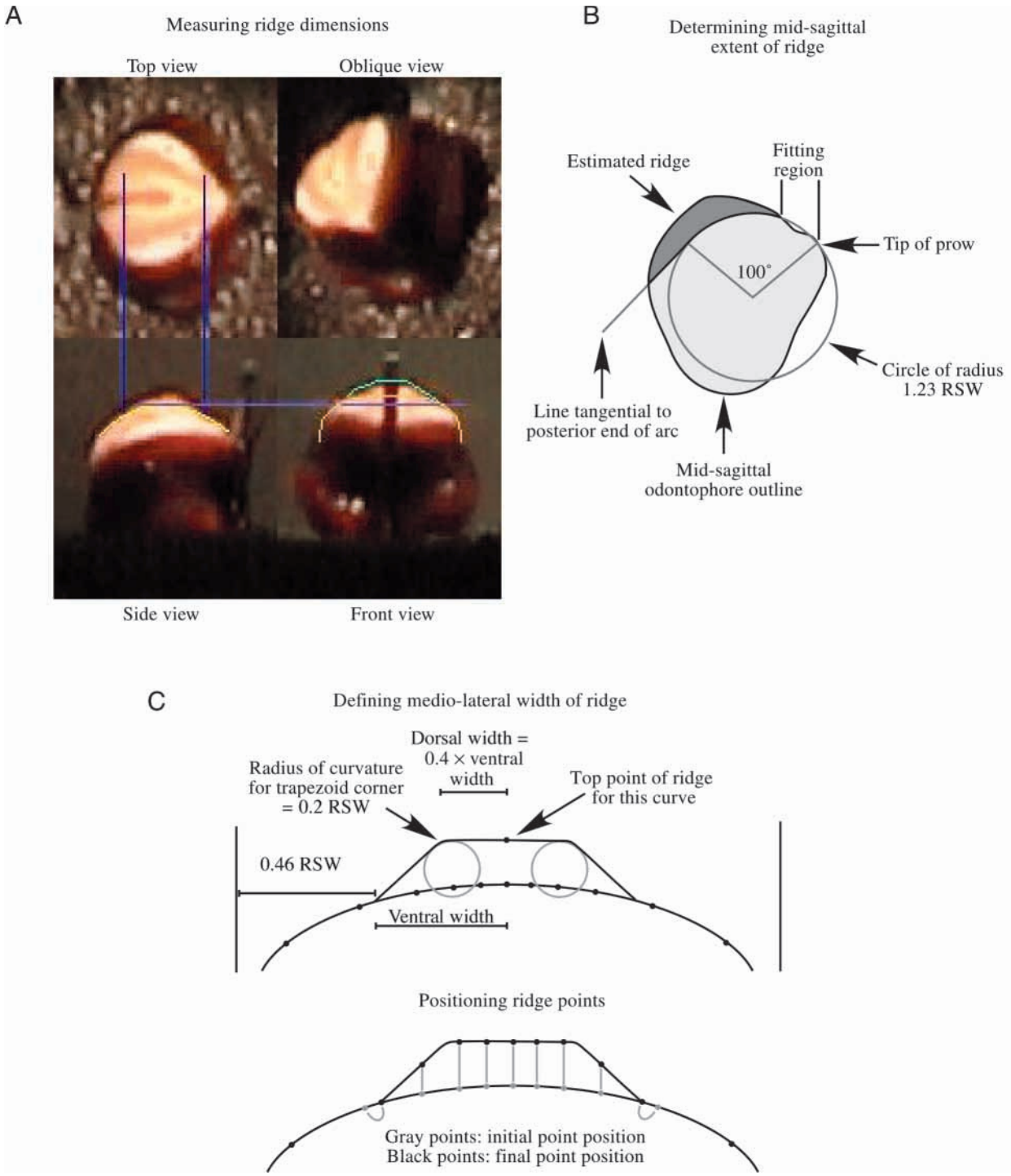

Fig. 5. Measurement and construction of the ridge. (A) Simultaneous top, side, front and oblique views are shown. Lines drawn on the different views indicate the extent of the ridge in these different views. In the front view, the lower line (yellow) indicates the spline curve defining the top of the odontophore not including the ridge, and the upper line (green) indicates the protrusion of the ridge above this curve. (B) A 100° arc of a circle whose radius is 1.23 radula stalk widths (RSW) (shown in grey) is a good fit to the radular surface below the region where the ridge occurs and is superimposed on the mid-sagittal outline of the odontophore extracted from the MRI to estimate the extent of the ridge. This curve is drawn in yellow on the side view of the radula in (A). The arc is continued posteriorly by a line tangential to the posterior end of the arc. (C) Implementation of the ridge. See Materials and methods for details.

above its maximum width; and *b2*, the height of the lumen below its maximum width. In the model I3 rings, the lumen is centered relative to the dorso-ventral length of the ring, but the widest point of the lumen and of the I3 ring need not be at the midpoint of the dorso-ventral length (i.e. *b1* and *b2* could have different values). Each ring can have a unique set of parameter values.

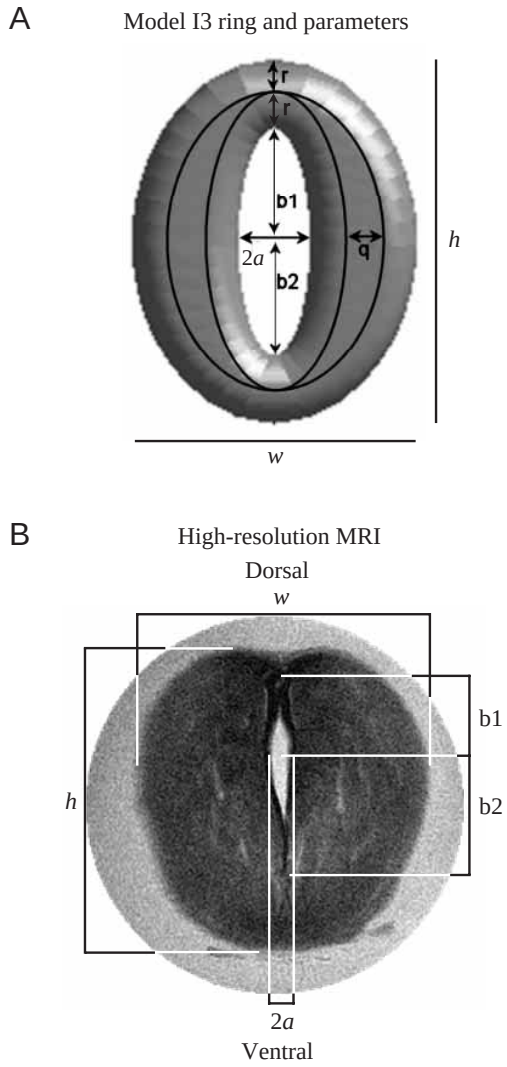

Fig. 6. Model I3 rings and parameter extraction from high-spatial-resolution MRIs. (A) Model I3 rings. The maximum width of the lumen is 2*a*, the height of the lumen above the maximum width is *b1*, and the height of the lumen below the maximum width is *b2*. The radius of the semi-circular cross section of the outer half-ring at the top and bottom and of the inner half-ring surrounding the lumen is *r*. The width added between the outer and inner half-rings so that the medio-lateral width matches that of the muscle at its widest extent, is *q*. The total height *h* of the model ring is equal to 4*r*+*b1*+*b2*, and its total width *w* is equal to 4*r*+2*q*+2*a*. (B) High-spatial-resolution MRI of the I3 muscle in axial section from an isolated buccal mass. The maximum lumen width, *a*, and of the heights below and above this maximum width (*b1* and *b2*, respectively), are shown on the image. In addition, the measurement of the maximum width, *w*, and maximum height, *h*, is illustrated. The parameter *r* is calculated from (*h*–*b1*–*b2*)/4, and the parameter *q* is calculated from (*w*–2*a*–4*r*)/2. The top and bottom borders of the lumen used in measuring *b1* and *b2* are measured from the dorsal and ventral extremes of the cartilage of the lumen, which appears black in the MRI because the lumen is partially closed. Measurements were made in pixels and then scaled to arbitrary model units. Note that, although lumen width 2*a* and muscle width *w* are not measured at the same dorso-ventral height, the calculation of *q* is performed as if they were at the same height. This follows from the model approximation (A), which assumes that the maximum lumen width and the maximum I3 ring width are at the same dorso-ventral height. Magnetic resonance acquisition parameters for the slice shown: fast spin echo, TE (time to echo)=120 ms, TR (time to repeat)=3000 ms, ETL (echo train length)=16, FOV (field of view)=5 cm×5 cm, SW (slice width)=1.5 mm, AM (acquisition matrix)=512×512, NEX (number of excitations)=4.

High-spatial-resolution MRI of anesthetized buccal masses indicated that the lumen was not necessarily centered along the dorso-ventral length and that the maximum medio-lateral width of the lumen was not necessarily coincident with the maximum medio-lateral width of the muscle (Fig. 6B). As a consequence, the following procedure was used to extract the five model parameters: (i) parameter *a* was determined by measuring the maximum width of the lumen and dividing by two; (ii) parameters *b1* and *b2* were determined by measuring the height of the lumen above and below its maximum width, respectively; (iii) the maximum dorso-ventral height (*h*) of the muscle was measured, and *r* was calculated as (*h*–*b1*–*b2*)/4, since, in the model, the total dorso-ventral height *h* of the I3 ring medially is 4*r*+*b1*+*b2* (Fig. 6A); (iv) the maximum medio-lateral width (*w*) of the muscle was measured, and *q* was calculated as (*w*–2*a*–4*r*)/2 since, in the model, the total medio-lateral width *w* of the I3 ring at its dorso-ventral midpoint is 4*r*+2*q*+2*a*.

The resting volume of the I3 rings served as a constraint for each ring so that, as a ring was placed around the odontophore during the feeding cycle, the ring's parameters were adjusted iteratively to maintain its constant volume. Parameter values for the model I3 rings, and their volume, were obtained from analysis of the resting anatomy of the I1/I3/jaw muscle. High-spatial resolution MRIs generated parameters for a series of 12 1.5 mm thick antero-posterior slices through the I3 muscle. Using the techniques described in the previous paragraph, a set of parameters was extracted for each of these 12 slices. This parameter set was then converted into resting parameters for an equivalent set of six model I3 rings using the following procedure. (i) Starting at the lateral groove, and starting with the *r* value of the slice closest to the lateral groove, all slices that were within a distance 2*r* of the lateral groove were analyzed and their parameters were averaged. (ii) Since, in general, this led to a new value of *r*, steps (i) and (ii) were repeated until the value of *r* stopped changing. (iii) Starting at the anterior end of the previous ring, steps (i) and (ii) were repeated for each additional ring until the *r* value estimated from the anatomy, multiplied by the number of remaining model rings, gave an antero-posterior distance that would not reach the jaws (in our measurements, this occurred for the fourth ring to be calculated, which is ring 3 in Table 1). For all remaining rings, a constant *r* value was then used so that the total thickness of the six model I3 rings would span the distance from the lateral groove to the jaws when the buccal mass was at rest. The parameters for the I3 rings with fixed

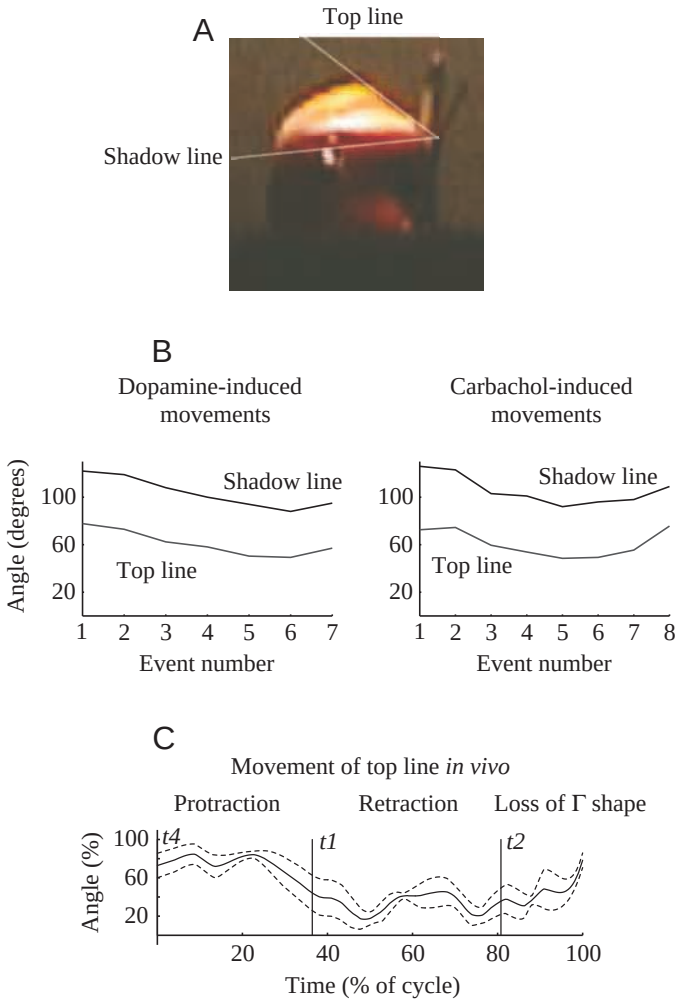

Fig. 7. Kinematics of the line of widest extent. (A) The line of widest extent is measured on the moving isolated odontophore as the line of dark shadow produced from a light source directly above the odontophore (shadow line). In addition, the line joining the tip of the prow and the top of the radula is measured (top line). The angles of the lines are measured relative to the line of the pin, which is the line connecting the tip of the prow with the bottom of the prow. (B) Comparison of the angle of the line of widest extent (shadow line) with the line connecting the tip of the prow and the top of the radula (top line) (measured in the side view). The two lines consistently differ by 44±5° (mean ± S.D., N=15). The left and right parts show data measured from an isolated odontophore induced to perform movements by application of dopamine or carbachol crystals (respectively) to the cerebral ganglion. Event 1, rest, closed radula; event 2, widest radular opening; event 3, immediately prior to radular closure; event 4, radular closure; event 5, odontophore elongation; event 6, maximum elongation; event 7, elongation relaxed. (C) Averaged and normalized changes in angle of the line connecting the top of the radula and the tip of the prow during four *in vivo* swallows. The feeding cycle was normalized on the basis of definitions of the components of the swallowing cycle from our previous work (Drushel et al., 1997, 1998; Neustadter et al., 2002). The time intervals for this and all subsequent figures are defined as follows, using the nomenclature adopted in our original papers for consistency: *t4*, start of anterior buccal mass movement to peak protraction; *t1*, peak protraction to peak retraction; *t2*, peak retraction to the loss of the Γ shape, i.e. the shape in which the base of the elongated radula/odontophore extends ventral to the long axis of the buccal mass (see fig. 3A of Drushel et al., 1997). Cycle times are normalized to the sum of the times *t4*+*t1*+*t2*. Lengths l were normalized to $100(l–l_{min})/(l_{max}–l_{min})$, so that lengths range from 0 at l_{min} to 100 at l_{max}. After normalization and averaging, the data were smoothed using an interpolation function that fitted cubic polynomials between successive data points. The average function is displayed as a solid line. A function representing ± 1 S.D. was calculated from the individual functions of the data and is displayed using dashed lines. The overall pattern of angular changes is similar to that observed *in vitro*.

r values were assigned by averaging the parameter values extracted from the equivalent MRI slices, based on the fixed r value. (iv) Finally, since the I3 and odontophore are anatomically attached by elastic tissue which stretches, and the six I3 rings are non-elastic, the calculated parameters were scaled (by 1.04) to model units such that the model I3 spanned the distance from the jaws to the lateral groove. The resulting parameter values are listed in Table 1.

Because both the high-spatial- and high-temporal-resolution MRIs showed that the inner margins of the I3 muscle were not straight lines, the I3 model was also modified to accept dorsal and ventral limit curves that could be arbitrary polynomials rather than straight lines. This made it possible to partially represent the ability of the I3 muscle to conform smoothly to the changing internal shape of the radula/odontophore, which was clearly visible in the mid-sagittal MRIs (e.g. see Fig. 9).

Iterative positioning algorithm

As demonstrated previously (Neustadter et al., 2002), the mid-sagittal MRI provides detailed information about the entire shape of the buccal mass during feeding. Instead of attempting to match two idealized features of the shape, the ellipticity and the eccentricity, as in previous models (Drushel et al., 1998, 2002), the present model attempted to match the entire irregular outline of the buccal mass. We implemented an iterative placement algorithm for this purpose, which met two constraints. First, the anterior I3 ring was required to meet the jaw line. Second, the outer border of the I3 rings had to match the outline of the buccal mass. The following degrees of freedom were modified if the I3 rings did not contact the jaw line or fit within the outline of the buccal mass: (i) the position of the hinge (i.e. the placement of the posterior I3 ring), which primarily affected the ventral placement of the I3 rings; (ii) the angle of the posterior ring relative to the odontophore, which primarily affected the dorsal placement of the I3 rings; and (iii) the polynomial limit lines, which primarily affected the match to the outline.

Results

We will present the experimental evidence for the kinematic relationships described in the Materials and methods section

and also discuss evidence that these aspects of the kinematics of isolated, intact odonotophores are similar to the kinematics of the odontophore *in vivo*. We will provide evidence suggesting that the improved model of the kinematics of the radula/odontophore leads to a more accurate model of the buccal mass. We will then use the model to describe the kinematics of specific buccal muscles (I2, I3 and I7) as well as the medio-lateral kinematics of the buccal mass that could not be observed in the mid-sagittal MRIs during the swallowing cycle (Neustadter et al., 2002).

Kinematic relationships for the radula/odontophore

To measure the location of the maximum medio-lateral width of the radula/odontophore throughout a feeding cycle, we examined the shadow cast by a light above the isolated odontophore. We observed that the shadow formed a line whose angle changed throughout the feeding-like movement cycle. We also noted that the line connecting the tip of the prow and the top of the radula had a fixed angle relative to the shadow line as it moved (Fig. 7A,B; the angle between the lines was 44±5°; mean ± S.D., N=15 measurements from two cycles). It is therefore possible to deduce the angle of the line of widest extent from the angle of the line connecting the tip of the prow to the top of the radula, which can be measured in mid-sagittal MRIs.

How do the kinematics of the line connecting the tip of the prow and the top of the radula compare between isolated odontophores and odontophores within the buccal mass during an *in vivo* swallowing movement? We examined this question by measuring the same line on odontophores during swallowing sequences *in vivo*. We observed that the line connecting the tip of the prow and the top of the radula showed very similar changes in angle throughout the cycle [Fig. 7C; the timing of the different *in vivo* behavioral periods (*t4*, *t1* and *t2*) used in this and subsequent figures is provided in the figure legend]. In turn, this suggests that inferences about the line of widest extent based on the experimentally defined kinematic relationship are likely to be valid throughout the feeding cycle *in vivo*.

We also characterized the kinematics of the large ridge that appears on the surface of the radula during feeding movements. After fitting a circular arc to the anterior portion of the radular surface (in a side view), the protrusion of the dorsal part of the odontophore above this arc correlated well with the ridge seen in a top view. Fig. 8A shows this relationship for several key frames for ridge protrusion in side and top views (r^2=0.84, P<0.002). Thus, one can use this kinematic relationship to deduce the anterior and posterior borders of the ridge and its height from the mid-sagittal MRIs.

How do the kinematics of the ridge observed in isolated odontophores compare with their kinematics in radula/odontophores within the buccal mass during swallowing *in vivo*? We determined the extent to which the ridge protruded above the radular surface in isolated odontophores as they underwent distinctive shape changes and compared them with the ridge area of odontophores during swallowing sequences *in vivo* (Fig. 8). Our measurements *in vitro* indicated that the

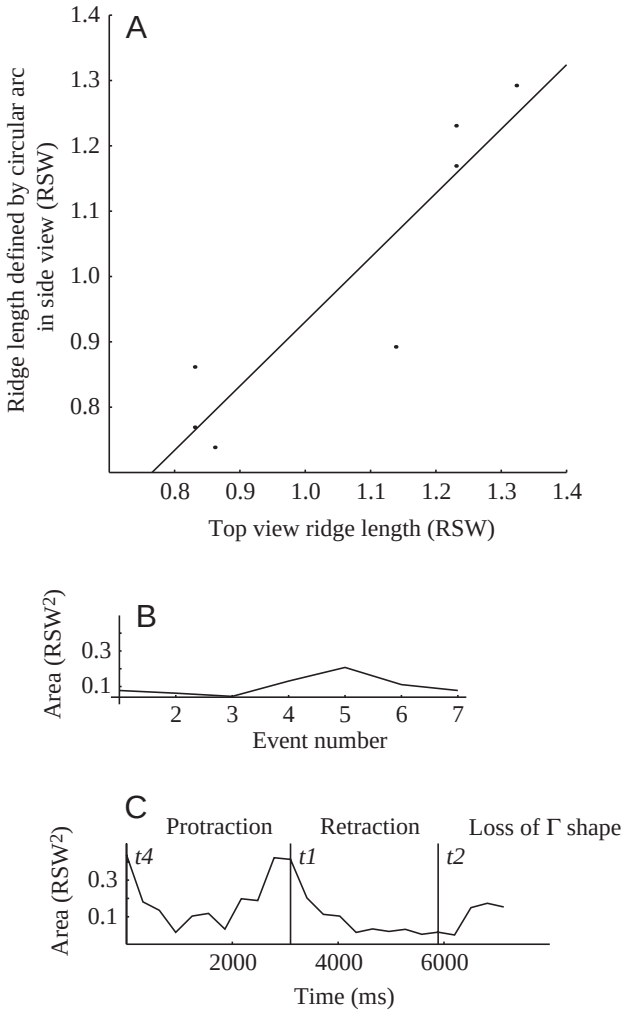

Fig. 8. Kinematics of the ridge. (A) Plot of the antero-posterior length of the ridge as seen in a top view *versus* the antero-posterior length of the protrusion of the ridge above a circular arc fitted to the odontophore in a side view (r^2=0.84, P<0.002). Fig. 5 shows one frame of these data and how they were analyzed. Lengths are measured in radular stalk width units (RSW). (B) Area of the ridge recorded *in vitro* during a dopamine-induced series of movements. See Fig. 7B for definitions of events labelled on the *x* axis. Area is reported in units of RSW^2. (C) Area of the ridge recorded *in vivo* from mid-sagittal frames (sequence 7732-S3, frames 16–39). Note the large ridge area at the end of protraction and at the onset of retraction, which corresponds to events 4 and 5 of the *in vitro* data, i.e. radular closure and odontophore elongation.

ridge was most prominent from the time that the radula closed and the odontophore elongated dorso-ventrally (event 4, Fig. 8B) until the time that the radular halves opened (event 6, Fig. 8B). On the basis of our previous analysis of the mid-sagittal *in vivo* kinematics (fig. 12, right side, in Neustadter et al., 2002), this corresponds to the early retraction phase of swallowing. Interestingly, the ridge area measured from *in vivo* mid-sagittal images reaches its maximum at the onset of retraction (Fig. 8C, border of *t4* and *t1* periods). In turn, this suggests that inferences about the ridge based on the

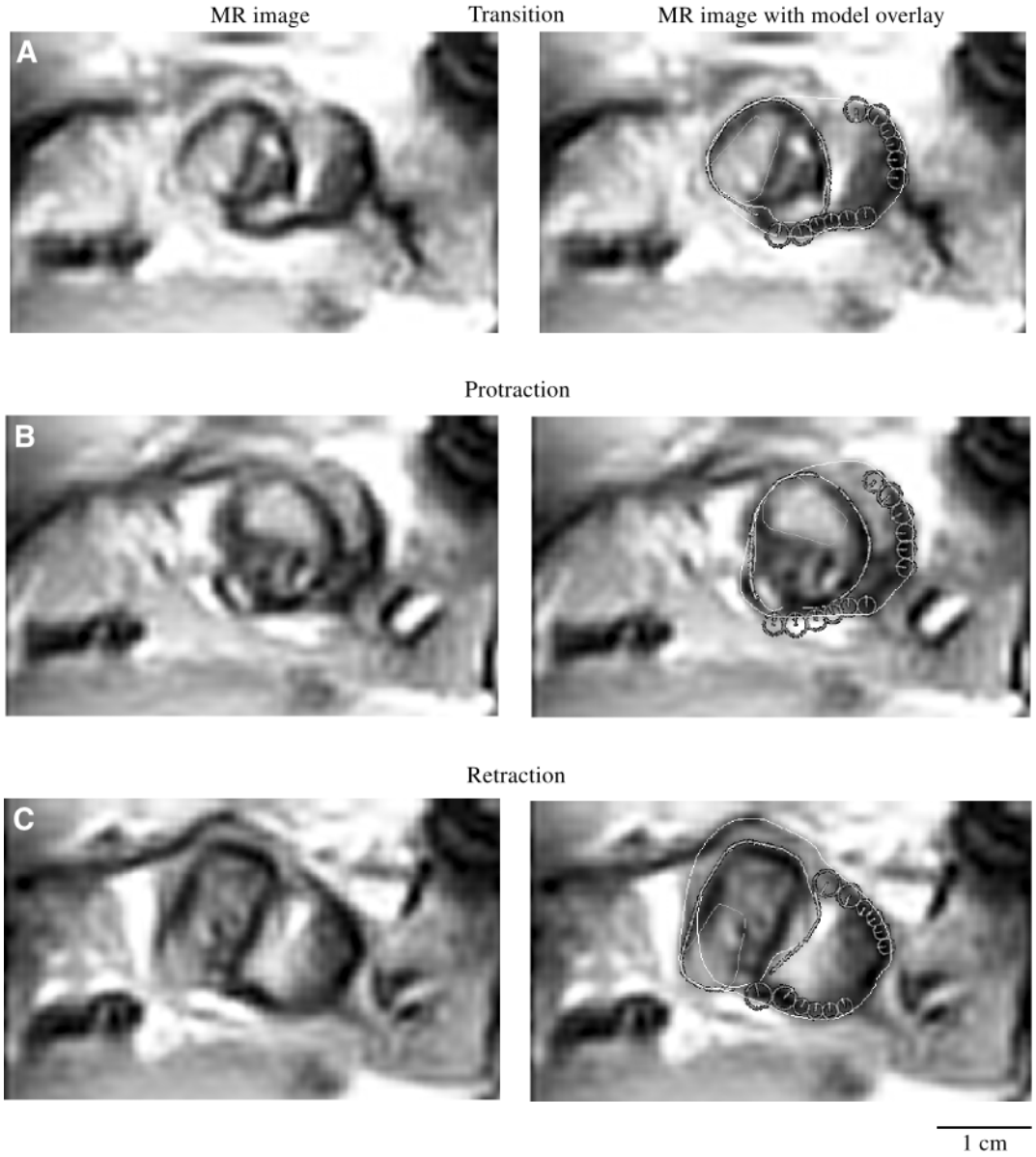

Fig. 9. Comparison of mid-sagittal magnetic resonance images (MRIs) (left) and superimposed mid-sagittal outputs (right) from the model. The frames shown are from sequence 7732-S3, frame 17 (A), sequence 7732-S3, frame 24 (B), and sequence 7732-S3, frame 35 (C). The outline of the odontophore, the outline of the radular stalk and the overall outline of the buccal mass were initially extracted from the MRIs shown on the left. The dorsal and ventral cross sections of the model I3 rings were placed by the model.

experimentally defined kinematic relationship are likely to be valid throughout the feeding cycle.

Model match to buccal mass kinematics

The kinematic model successfully matched the mid-sagittal outlines of the buccal mass measured from the high-temporal-resolution MRIs (Fig. 9). The only significant mismatches occurred in the posterior rings of the I3 muscle, which often extended beyond the outline of the buccal mass. This mismatch is due to an inherent limitation of the current I3 model (see Discussion).

The most important assumption of the model was that kinematic relationships derived from isolated radula/odontophores performing feeding-like movements *in vitro* would generate valid predictions for the medio-lateral width of the radula/odontophore throughout the feeding cycle *in vivo*. It was possible to test this critical assumption because, during data acquisition, mid-sagittal MRIs were interleaved with axial and coronal images of the buccal mass (Neustadter et al., 2002). By sectioning the three-dimensional model buccal mass at the location of the corresponding coronal MR slice, it was possible to generate coronal slices through the model that could be directly compared with coronal MRIs (Fig. 10). Because the coronal images were temporally interleaved between the mid-sagittal images (see Neustadter et al., 2002), we compared each coronal image with the model frame based on the mid-sagittal image

preceding the coronal image, with the model frame following the coronal image and with a combination of the preceding and following model frames, and used the best match for the comparison. A quantitative test of the validity of the model was performed by computing the symmetric difference (Alt et al., 1998) between the outlines of the MR and model images as a percentage, i.e. 100(union – intersection)/union. Ten sets of images that were correctly matched generated a mean error of 13±2% (mean ± S.D., N=10). In contrast, 10 pairs of randomly matched images generated a mean error of 19±7% (mean ± S.D., N=10). A Kolmogorov–Smirnov test (Sokal and Rohlf, 1981) comparing the error distributions in ordered *versus* randomized comparisons suggested that they were different (P=0.014). A qualitative test of the validity of the model was also performed by giving seven human volunteers 11 MRI shapes and 11 model shapes (taken from sequence 7732, using every other frame from 18 to 38, inclusive) and asking each volunteer to pair the images so that they matched (a subset of the shapes presented is shown in Fig. 10). Errors were quantified by computing the difference between the frame number of a given MRI shape and the frame number of the corresponding model shape assigned by the human subject and summing this error over all 11 possible matches. Thus, a subject who assigned all model shapes to the correct MRI shapes would receive a score of 0, and a subject who consistently missed all matches by one frame would receive a score of 11. Actual error scores were 9.6±2.8 (N=7, mean ± S.D.), suggesting that subjects could match model shapes to MRI shapes within one frame or better, on average. No subject's match was off by more than two frames. These results suggest that the model effectively captures changes in the medio-lateral shape of the buccal mass throughout the feeding cycle.

Buccal mass kinematics

The mid-sagittal and coronal matches between the model and the MRIs suggest that the overall three-dimensional shape of the buccal mass is captured well by the model (Fig. 11). The lateral views of the three-dimensional reconstruction (Fig. 11A) are in the same orientation as the original mid-sagittal images (Fig. 9). The dorsal and anterior views (Fig. 11B,C) have been rotated so that the lateral groove (the posterior edge of the model I3 musculature) is perpendicular to the plane of the page. Fig. 11A and Fig. 11B can be compared with the outputs of the previous odontophore-centric model (fig. 9G–I and fig. 9J–L, respectively, in Drushel et al., 2002). For the purpose of the discussion of the dimensions of the odontophore, the reference frame is such that the line defining the attachment of the prow to the I6 muscle is vertical. Thus, the ridge is dorsal, the radular sac is ventral and the prow is anterior.

During transition (Fig. 11, left column), the odontophore is widest in the medio-lateral direction and narrowest in the dorso-ventral direction, compared with protraction and retraction, and the radular stalk is deep within the odontophore, suggesting that the radular halves are open. At peak protraction (Fig. 11, middle column), the odontophore is narrower medio-laterally than it is at transition, suggesting that the odontophore may be compressed by the I1/I3/jaw musculature. Shortly thereafter, the radular stalk moves out of the odontophore, suggesting that the radular halves are closing. At peak retraction (Fig. 11, right column), the radular stalk has moved out of the odontophore,

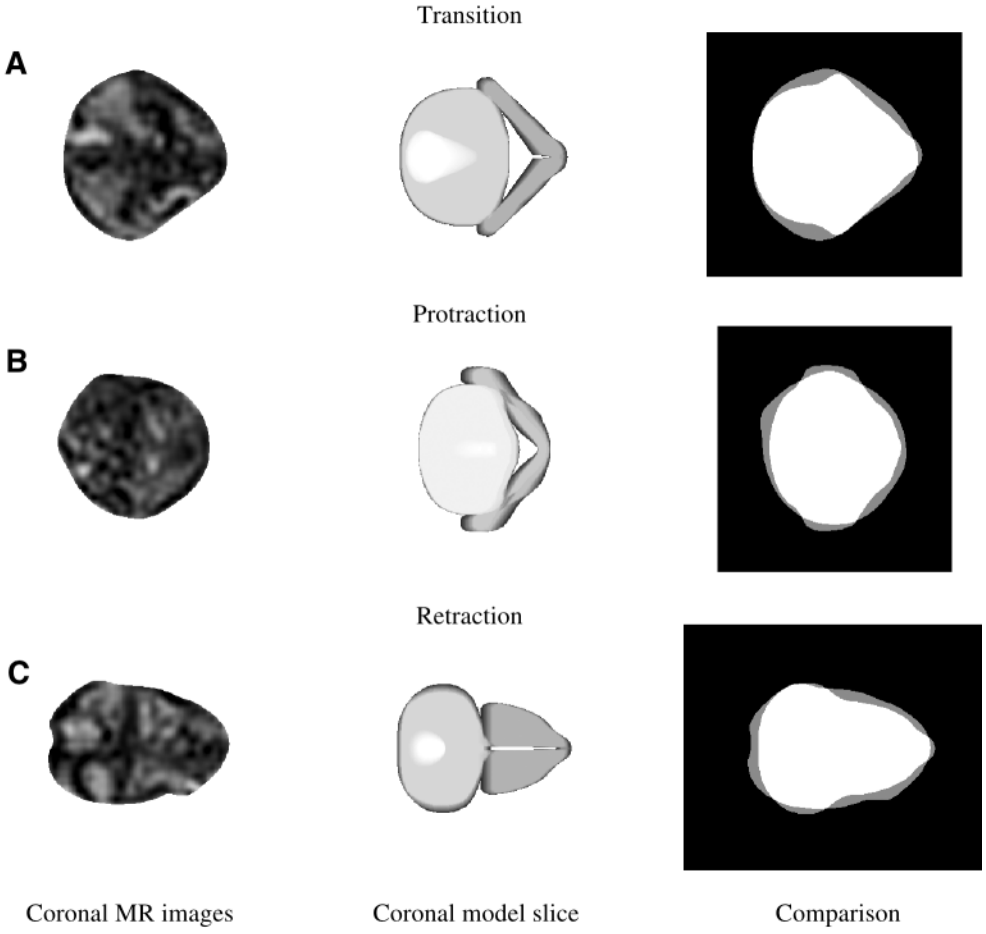

Fig. 10. Validation of the model using coronal sections. In each row, the sequence of images is the interleaved coronal MRI, the coronal slice through the three-dimensional model and the symmetric difference between them. In the images showing the symmetric differences, white indicates areas that are in both coronal images, whereas grey indicates areas that differ. (A) Transition; sequence 7732-S3, frame 18. (B) Peak protraction; sequence 7732-S3, frame 24. (C) Peak retraction; sequence 7732-S3, frame 36.

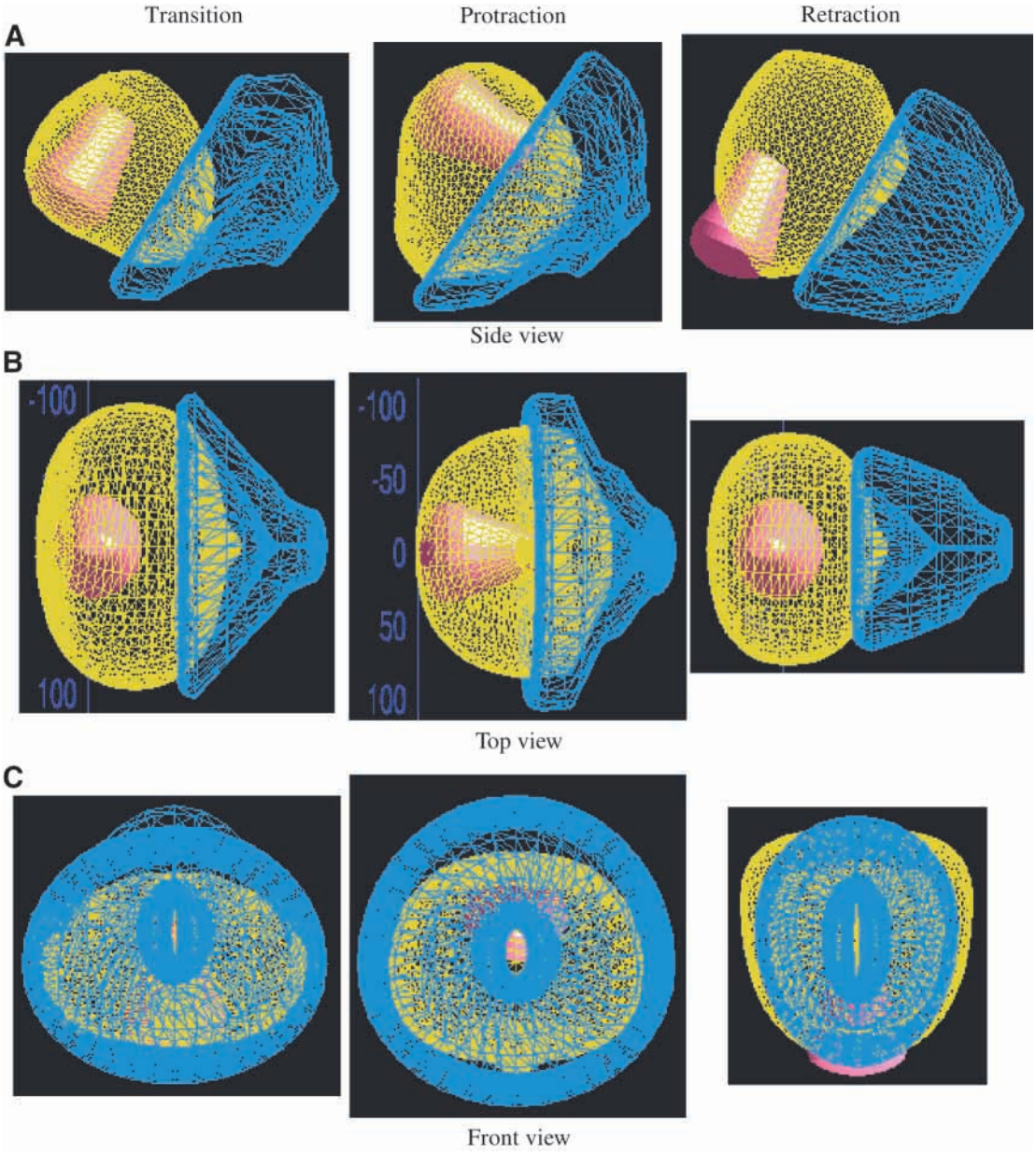

Fig. 11. Three-dimensional reconstruction of the buccal mass during a swallowing cycle. The I1/I3 muscles are shown as a continuous blue mesh, the odontophore is shown as a continuous yellow mesh and the radular stalk is shown as a red solid. Views are shown in orthographic projection. (A) Side views of transition, protraction and retraction. Compare the mid-sagittal slices shown in Fig. 9. (B) Top view of transition, protraction and retraction. Compare the coronal slices shown in Fig. 10. To generate these views, the lateral groove (posteriormost edge of the I1/I3/jaw muscle complex) has been rotated so that it is vertical. (C) Front view of transition, protraction and retraction. The left, middle and right columns are based on frames 17, 24 and 35, respectively, of sequence 7732-S3. Compare fig. 9 of Drushel et al. (2002), which shows a three-dimensional reconstruction of a previous odontophore-centric model of the buccal mass for sequence 7732-S3, frames 15 (left), 26 (middle) and 35 (right).

which is now longer in the dorso-ventral direction and much narrower in the medio-lateral direction, suggesting that the radular halves are strongly closed together.

Kinematics of buccal muscles I2, I3 and I7

I2 kinematics

Another means of verifying the model of the buccal mass is to compare its predictions about the changes in the length of a protractor muscle, the I2 muscle (Hurwitz et al., 1996), with *in vivo* measurements during a swallowing cycle derived from high-temporal-resolution MRIs (Neustadter et al., 2002). We compared these results with estimates of the I2 length derived from the model by measuring the arc length of the posterior outline of a mid-sagittal cross section of the three-dimensional model from the dorsal surface of the most posterior I3 ring to the ventral surface of the most posterior I3 ring (Fig. 12; model

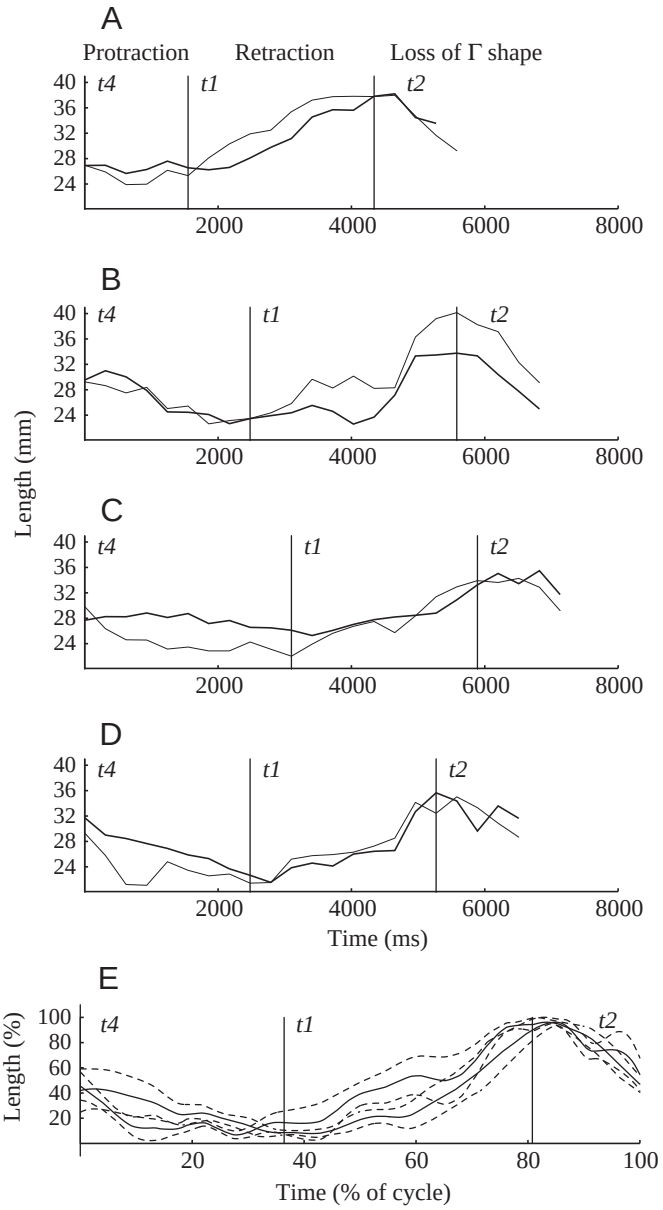

Fig. 12. Kinematics of the I2 muscle predicted by the model and compared with I2 lengths measured in the same magnetic resonance images (MRIs). Data in A–D are plotted as length (mm) as a function of time (ms). Data from the model are plotted using a black line; data measured from MRIs are plotted using a grey line. Frame numbers for sequences and for the onset of *t4*, *t1* and *t2* periods are given in Neustadter et al. (2002) and in the legend to Fig. 7. (A) I2 kinematics in the first swallow. (B) I2 kinematics in the second swallow. (C) I2 kinematics in the third swallow. (D) I2 kinematics in the fourth swallow. (E) Normalized, averaged and smoothed I2 kinematics during a swallowing cycle. Values are means ±1 S.D. (*N*=4).

results are shown in black, MRI data from the same swallow are shown in grey). Qualitatively, the changes in length are very similar, reaching a maximum near peak retraction and a minimum near peak protraction. Quantitatively, the model measurements do not exactly match the MRI measurements. The model predicts too long a length for peak protraction in two swallows (Fig. 12C,D; middle of *t4* period), too short a length during retraction for two swallows (Fig. 12A,B; *t1* period) and too short a length for peak retraction in one swallow (Fig. 12B; onset of *t2* period). The average normalized values for the actual MRI data and the model are close, except for a consistent overestimate of the length during protraction (Fig. 12E; *t4* period) and an underestimate of the length predicted during retraction (Fig. 12E; *t1* period). Despite these discrepancies, the overall shape of the I2 measurements are similar in the model, in the MRIs, and in estimates from transilluminated juvenile animals (Fig. 7 in Neustadter et al., 2002).

I3 kinematics

The I3 muscle plays an important role in mediating retraction during swallowing (Morton and Chiel, 1993a). Predictions of the model for the antero-posterior length of I3 on the dorsal and ventral surfaces and for the dorso-ventral length of I3 at the lateral groove and at the jaws can be compared with actual lengths of I3 measured directly from the original MRIs (Neustadter et al., 2002). The antero-posterior lengths of I3 along the ventral surface of the buccal mass are reasonably well-matched to those measured from the MRIs (Fig. 13, right-hand plots). In contrast, the antero-posterior length of I3 on the dorsal surface is consistently overestimated in three of the four swallows, especially late in protraction and during much of retraction (Fig. 13, left-hand plots; only the third swallow, Fig. 13C, matches the *in vivo* data well throughout the cycle). The dorso-ventral lengths of I3 at the lateral groove and at the jaw are matched very well by the model throughout the swallowing cycle (Fig. 14, left-hand and right-hand plots).

In previous studies, we measured the medio-lateral width of the I3 jaw musculature at several locations along its antero-posterior length from dorsal views of transilluminated juvenile slugs (Drushel et al., 2002). Because the MRIs are cross sections of the buccal mass rather than projections and do not necessarily cross through the widest plane of the buccal mass, it is not possible to use the coronal MRIs to compare these results directly. However, it is possible to measure these widths in the three-dimensional kinematic model. Estimates of the widths of I3 from kinematic model runs of four different swallows (Fig. 15A–D) are compared with measurements of the widths of I3 from three successive swallows of a transilluminated juvenile *Aplysia californica* (Fig. 15E,F). Both methods of measuring the I3 widths suggest that there are significant variations in the pattern of width changes in the muscle from swallow to swallow. The model reproduces two important features of the *in vivo* data: (i) the changes in the widths are smooth throughout the cycle, unlike previous models that generated abrupt width changes when the odontophore entered or left the I3 muscle; and (ii) the resting distribution of the widths and their overall shape during the cycle are similar to the *in vivo* data, which is also an improvement over previous models. One

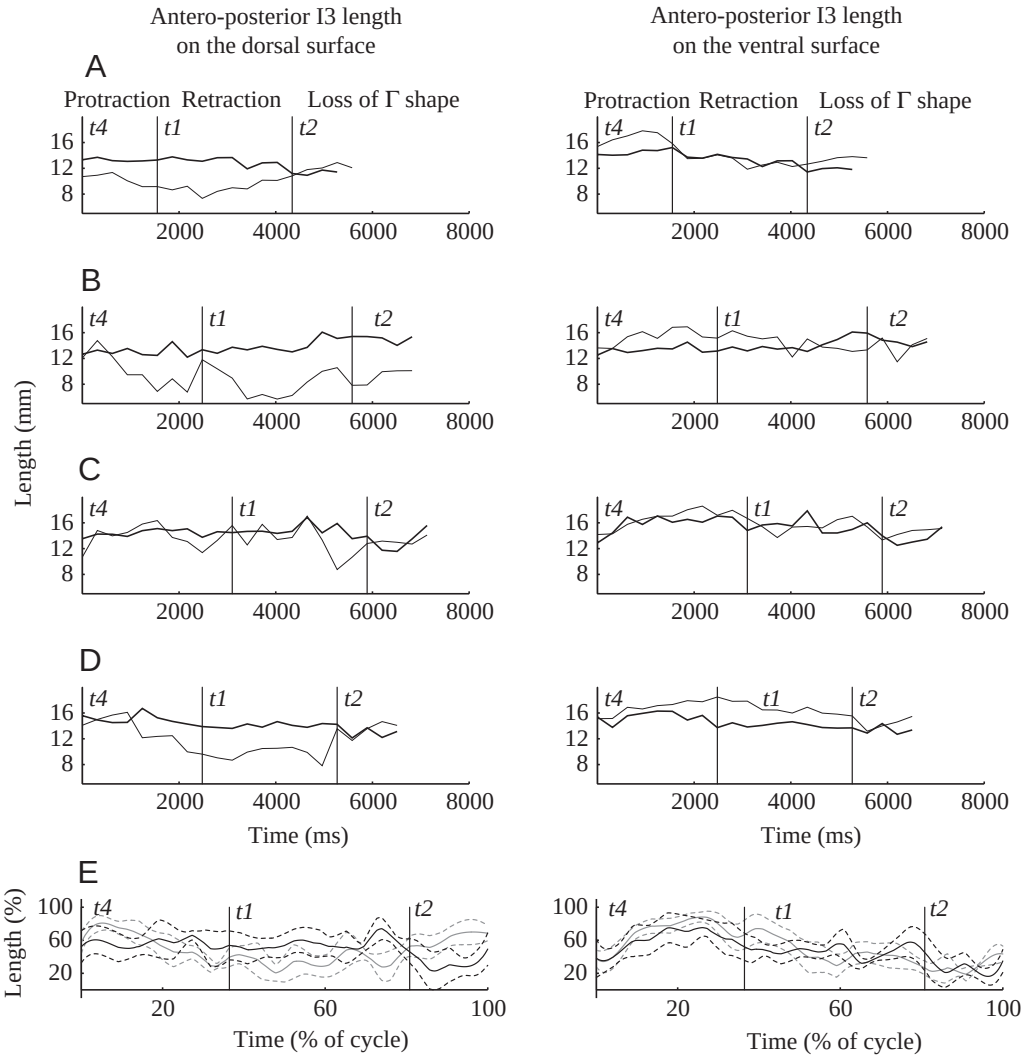

Fig. 13. Kinematics of the antero-posterior lengths of the I3 muscle compared with measurements in the same magnetic resonance images (MRIs). Data in A–D are plotted as length (mm) as a function of time (ms). Data from the model are plotted using a black line; data measured from the MRIs are plotted using a grey line. On the left side are plots of the antero-posterior I3 length on the dorsal side of the model. On the right side are plots of the antero-posterior I3 length on the ventral side of the model. The match to the lengths on the ventral surface is good but, in three out of the four swallows, the match to the antero-posterior length of I3 on the dorsal surface is poor, especially during late protraction and most of retraction. (A) I3 antero-posterior kinematics in the first swallow. (B) I3 antero-posterior kinematics in the second swallow. (C) I3 antero-posterior kinematics in the third swallow. (D) I3 antero-posterior kinematics in the fourth swallow. (E) Normalized, averaged and smoothed I3 antero-posterior kinematics during a swallowing cycle. Values are means ±1 S.D. (*N*=4). At the protraction/retraction transition and early in retraction (*t4/t1* transition and early *t1*), the model underestimates the length of the ventral surface because of its inability to represent stretch of the ventral I3 muscle around the prow.

difference between the data sets is that, in the data from the transilluminated animal, the relative change in width is greatest for the most anterior part of I3 (near the jaws; lowest traces in Fig. 15E–G) and smallest for the most posterior part of I3 (near the lateral groove; top traces in Fig. 15E–G). In contrast, in the data from the kinematic model, at least for the first, third and fourth swallows, the relative change in width is greatest for the region of I3 nearest the lateral groove and smallest for the region of I3 nearest the jaws (Fig. 15A–D).

The second sequence of data generated by the model is different from the other three sequences. During this swallow, the animal strongly protracted the radula/odontophore (fig. 11B in Neustadter et al., 2002; note the prolonged and very strong forward translation and rotation of the odontophore in the second swallow). At the same time, the estimated medio-lateral width of the odontophore is narrower than that observed during other swallows throughout retraction (see Fig. 17B; compare with Fig. 17A,C,D). These observations suggest that the animal strongly closed its radular halves after its very strong protraction. These data suggest that measurements of I3 width may be very sensitive to the shape of the radula/odontophore.

I7 kinematics

Previous studies in isolated buccal masses have demonstrated that the I7 muscle can act as a radular opener (Evans et al., 1996). Using the model, we estimated the kinematics of the I7 muscle throughout the swallowing cycle. On the basis of its anatomy, we defined the I7 muscle in the model as extending from the anteriormost point on the seam between the radular sac and the radular stalk to the top of the prow seam, which is indicative of the dorsal anterior edge of the I6 muscle. Because the position of the prow seam is iterated to obtain the correct volume for the prow, the location of the anterior tip of I7 was set by the model, although in general it was close to the location initially determined directly from the mid-sagittal MRIs. The most significant changes in I7 are its

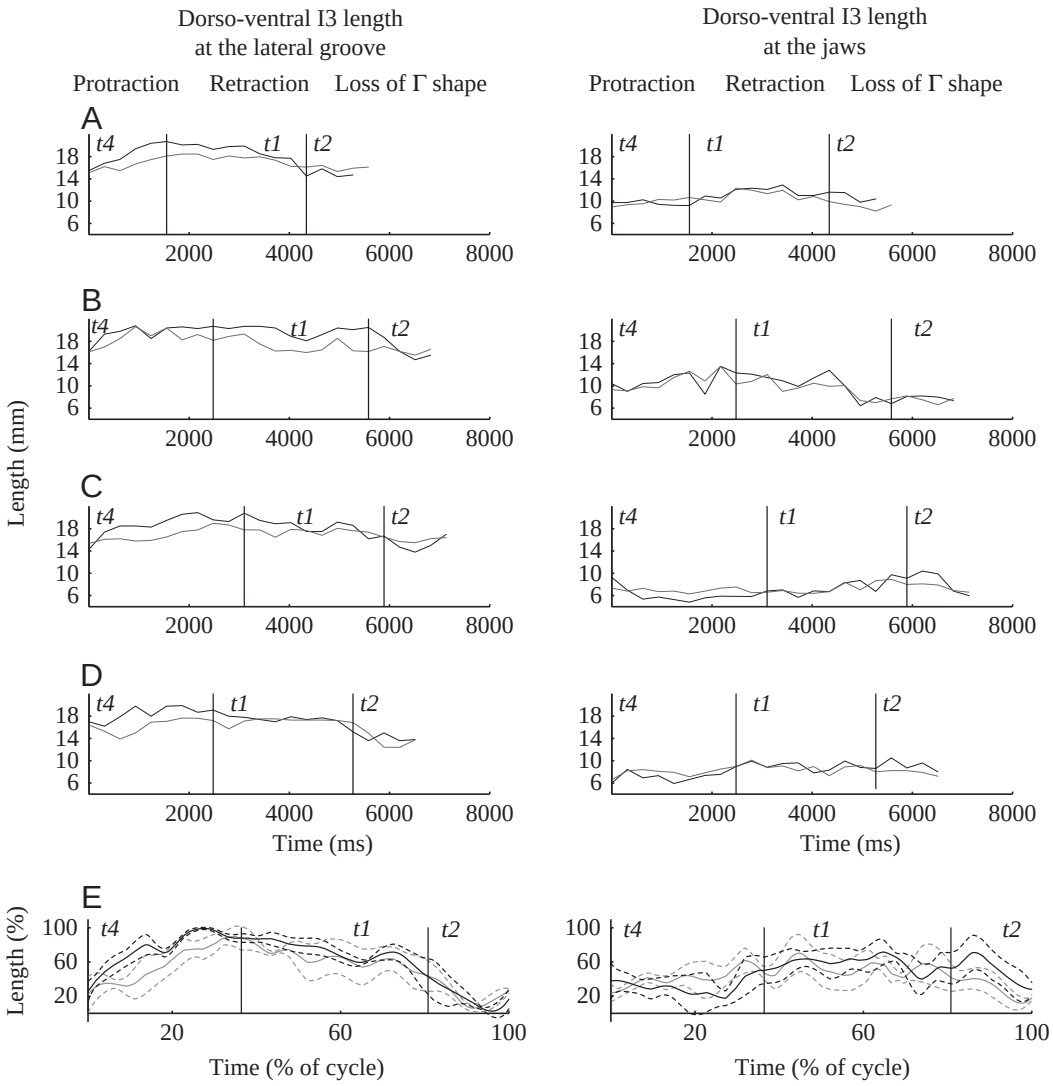

Fig. 14. Kinematics of the dorso-ventral lengths of the I3 muscle compared with measurements in the same magnetic resonance images (MRIs). Data in A–D are plotted as length (mm) as a function of time (ms). Data from the model are plotted using a black line; data measured from the MRIs are plotted using a grey line. On the left side are plots of the dorso-ventral I3 length at the lateral groove. On the right side are plots of the dorso-ventral I3 length at the jaws. The match between the model and measured data is excellent for all four swallows throughout the swallowing cycle. (A) I3 dorso-ventral kinematics in the first swallow. (B) I3 dorso-ventral kinematics in the second swallow. (C) I3 dorso-ventral kinematics in the third swallow. (D) I3 dorso-ventral kinematics in the fourth swallow. (E) Normalized, averaged and smoothed I3 dorso-ventral kinematics during a swallowing cycle. Values are means ±1 S.D. (*N*=4). Note the overall match in the right-hand and left-hand plots between the average model data and the average MRI data. The model overestimates the dorso-ventral length of I3 at the lateral groove during protraction (*t4* period, left).

lengthening from the peak of protraction to the peak of retraction (Fig. 16, *t1* period), and then its rapid shortening just after the peak of retraction, prior to the onset of protraction (Fig. 16, *t2* period). In all four sequences, there is a smaller lengthening and shortening of I7 during the protraction phase (Fig. 16A–D, *t4* period).

Radula/odontophore kinematics during swallowing

By using the kinematic relationships and the kinematic model, it is possible to infer the kinematics of the radula/odontophore in the medio-lateral dimension. The maximum half-width of the odontophore in the medio-lateral direction decreases steadily during protraction (Fig. 17, *t4* period), is smallest after peak protraction and during the early retraction phase (Fig. 17, *t1* period) and is largest after the collapse of the Γ shape of the radula/odontophore (Drushel et al., 1997) (Fig. 17; end of *t2* period). The ridge is largest during the late protraction and early retraction phases and is not visible during middle to late retraction (Fig. 8C shows data for one swallow). The prow is largest in antero-posterior thickness during protraction, decreases to a minimum during retraction and increases in thickness during the collapse of the Γ shape (averaged data for four swallows are shown in Fig. 18; panel labelled ‘Prow size’).

Discussion

In this paper, we have investigated the constraints on the kinematics of the radula/odontophore based on measurements of isolated, intact odontophores. This has led us to analyze kinematically components of this structure – the prow and the ridge – that have not been previously characterized. By extracting kinematic relationships from the studies of the isolated radula/odontophore and parameters from high-temporal-resolution MRIs, we have created a more detailed kinematic model of the buccal mass than any previously described (Drushel et al., 1998, 2002). The similarity between the kinematics of key features measured from odontophores during swallowing using MRI and those measured from isolated odontophores suggests that the kinematic relationships inferred in isolated radula/odontophores are of value for understanding the kinematics of the radula/odontophore in the context of the entire buccal mass. The excellent match between the model's predictions of the shapes of the buccal mass in the coronal plane and actual MRIs in the coronal plane supports the hypothesis that the three-dimensional shape of the intact buccal mass is largely determined by the three-dimensional shape of the radula/odontophore.

Limitations of the kinematic model

Examination of the detailed differences between the mid-sagittal MRIs and the mid-sagittal model cross sections indicates that the most significant discrepancies in this dimension are due to the limitations of the current I3 muscle model. In the comparison of the coronal MRIs and model coronal cross sections, the lack of widening at the jaws during early protraction in the model relative to that seen in the MRI is due primarily to the independence of the I3 rings in the model. In the biological system, the stiffness of the underlying cartilage, the tension provided by the overlying I1 muscle and the large number of deforming I3 muscle bands act to move the musculature in a more uniform way, inducing more uniform expansions or contractions of the I1/I3/jaw musculature. In the model, the I3 rings represent the I3 muscle at much lower spatial resolution and move independently and are, thus, much more affected by the local cross section of the odontophore protruding through them. In the model, the ring at the jaws will not expand significantly until the odontophore protrudes through it, whereas in the biological system the expansion of the more posterior regions of the musculature will cause the jaw region to expand even if the odontophore is not protruding through it.

The I3 antero-posterior lengths on the dorsal side are consistently too long in the model compared with the MRIs (Fig. 13, left side). The errors are the result of two factors. First, the model does not provide independent control of the dorsal and ventral thicknesses of the I3 rings, which are clearly different, as seen in the high-spatial-resolution MRIs (Fig. 6). Second, the ventral length of I3 is constrained to fit between the line of the jaws and the antero-ventral surface of the odontophore, i.e. the hinge point. In the biological system, the ventral side of I3 is sometimes stretched and therefore becomes longer than the dorsal side, which cannot be reproduced by our model, leading to a significant error in the antero-posterior length of the dorsal side. The model's overestimate of the

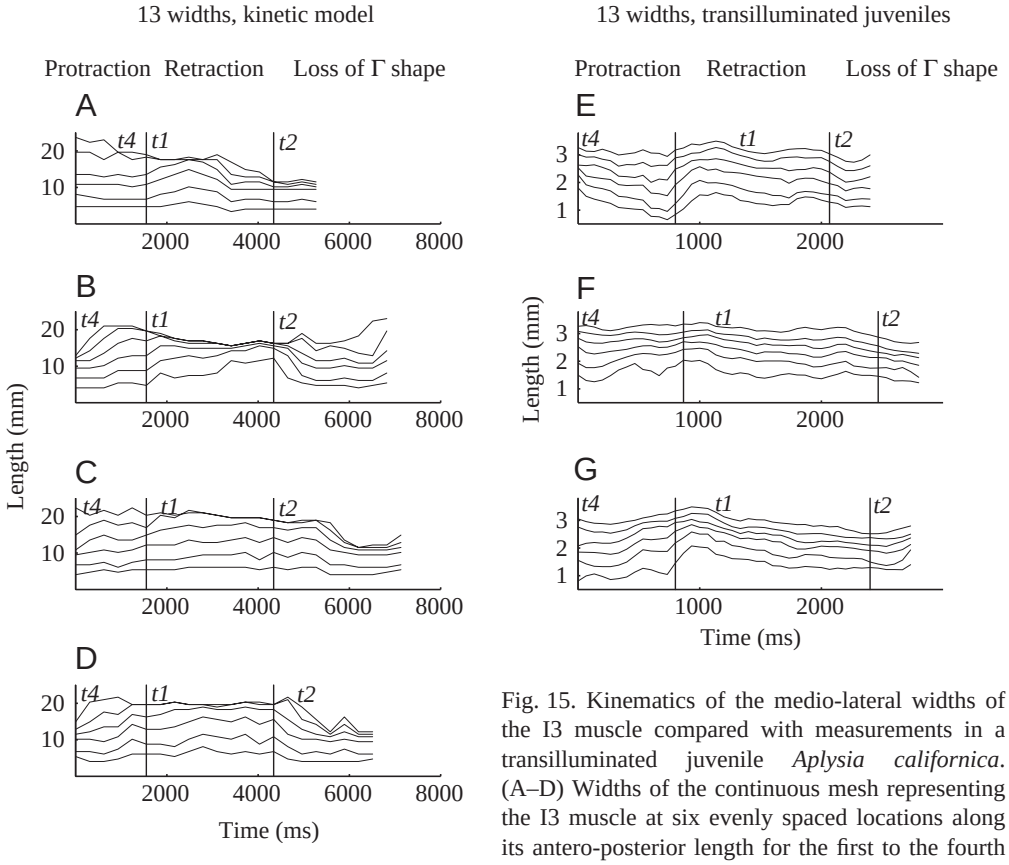

Fig. 15. Kinematics of the medio-lateral widths of the I3 muscle compared with measurements in a transilluminated juvenile *Aplysia californica*. (A–D) Widths of the continuous mesh representing the I3 muscle at six evenly spaced locations along its antero-posterior length for the first to the fourth swallows; (E–G) widths of the I3 muscle measured at six evenly spaced locations along its antero-posterior length from dorsal views of transilluminated juveniles in three successive swallows, as described in the legend to fig. 6A in Drushel et al. (2002). Data in E–G are smoothed using a moving average over three successive data points and are plotted as length (mm) as a function of time (ms). The top trace in each set of six traces is the medio-lateral width of I3 at the lateral groove, whereas the bottom trace in each set corresponds to the medio-lateral width of I3 at the jaws. Variability from swallow to swallow is evident both in the traces generated by the model and in the measurements from the transilluminated juvenile animal.

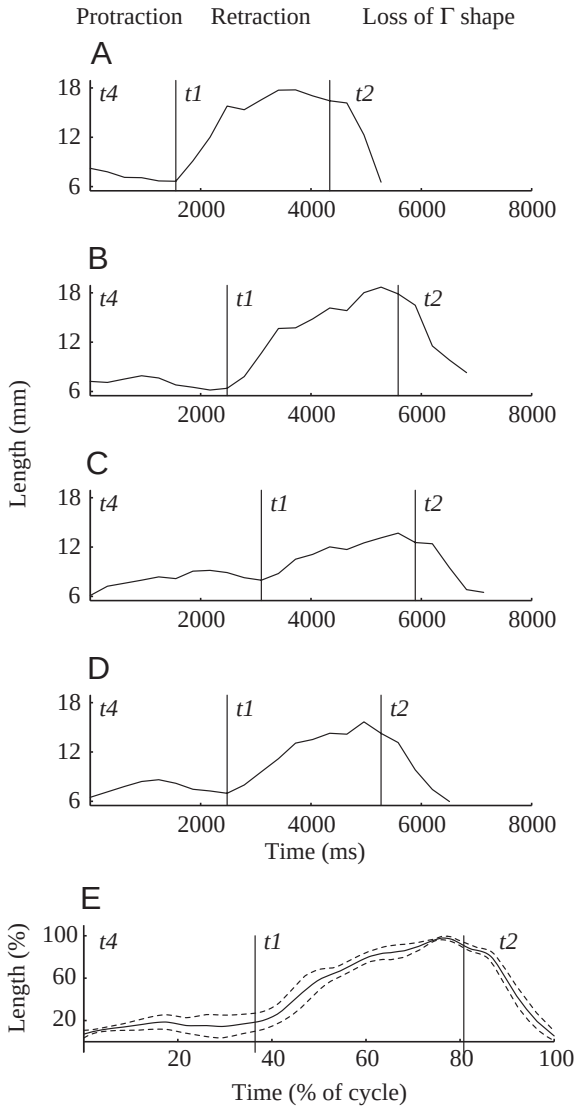

Fig. 16. Kinematics of the I7 muscle estimated from the model. Data are plotted as length (mm) as a function of time (ms). (A) I7 length in the first swallow. (B) I7 length in the second swallow. (C) I7 length in the third swallow. (D) I7 length in the fourth swallow. (E) Normalized, averaged and smoothed I7 length during a swallowing cycle. Values are means ±1 S.D. (*N*=4).

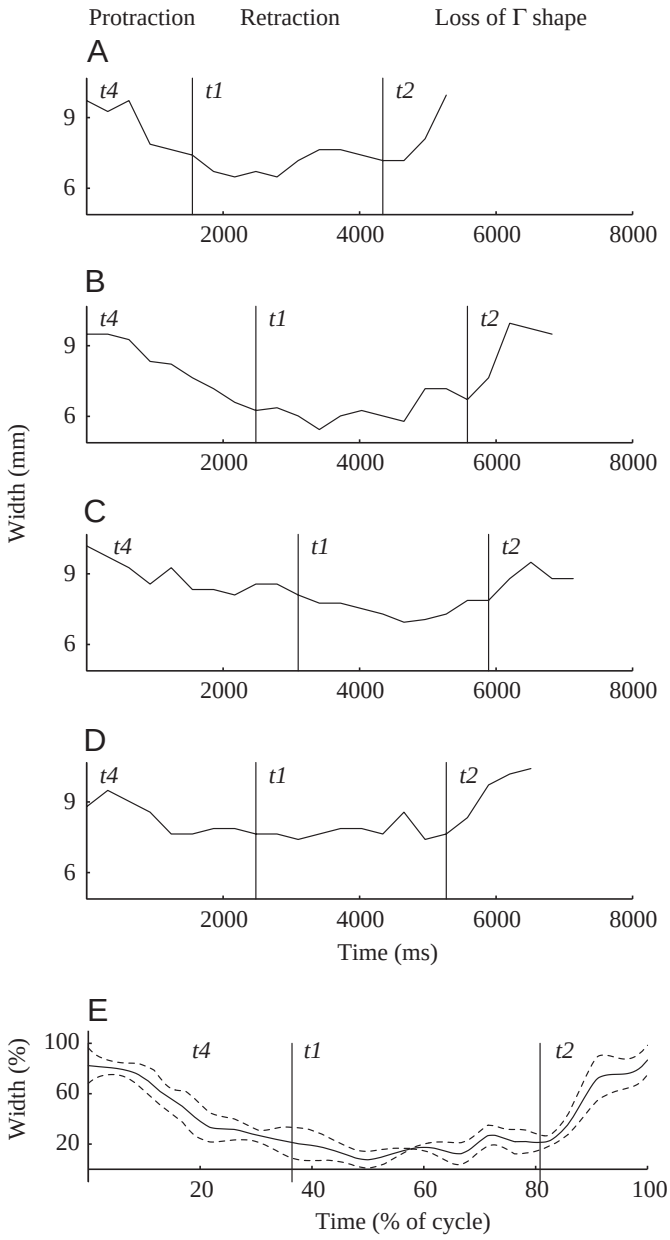

Fig. 17. Kinematics of the medio-lateral half-width of the odontophore estimated from the model. Data are plotted as width (mm) as a function of time (ms). Half the width of the odontophore is plotted, since this provides an estimate of the width of one of the paired I4 muscles, which constitute most of the width of the odontophore. (A) Medio-lateral half-width in the first swallow. (B) Medio-lateral half-width in the second swallow. (C) Medio-lateral half-width in the third swallow. (D) Medio-lateral half-width in the fourth swallow. (E) Normalized, averaged and smoothed medio-lateral odontophore half-width during a swallowing cycle. Values are means ±1 S.D. (*N*=4).

antero-posterior I3 length on the dorsal side is likely to account for the underestimate in I2 length during retraction (for example, for swallow 2, note the errors in Fig. 13B on the left side and in Fig. 12B near the *t1/t2* transition). The inability of the ventral side of the I3 rings to stretch over the prow also causes the model to predict that I2 is longer than it actually is during the protraction phase. This suggests that we need to create a new model of the I1/I3 jaw musculature with higher spatial resolution and greater anatomical accuracy and to characterize the kinematic relationships between the mid-sagittal cross sections of the I3 muscle and its medio-lateral deformations in a study similar to that described in the present paper for the radula/odontophore.

Another limitation of the current radula/odontophore model is that it does not incorporate the radular cleft, i.e. the space between the radular halves. In the retraction phase of swallowing, during which the radular halves are in contact with one another and there is no cleft, this simplification is not

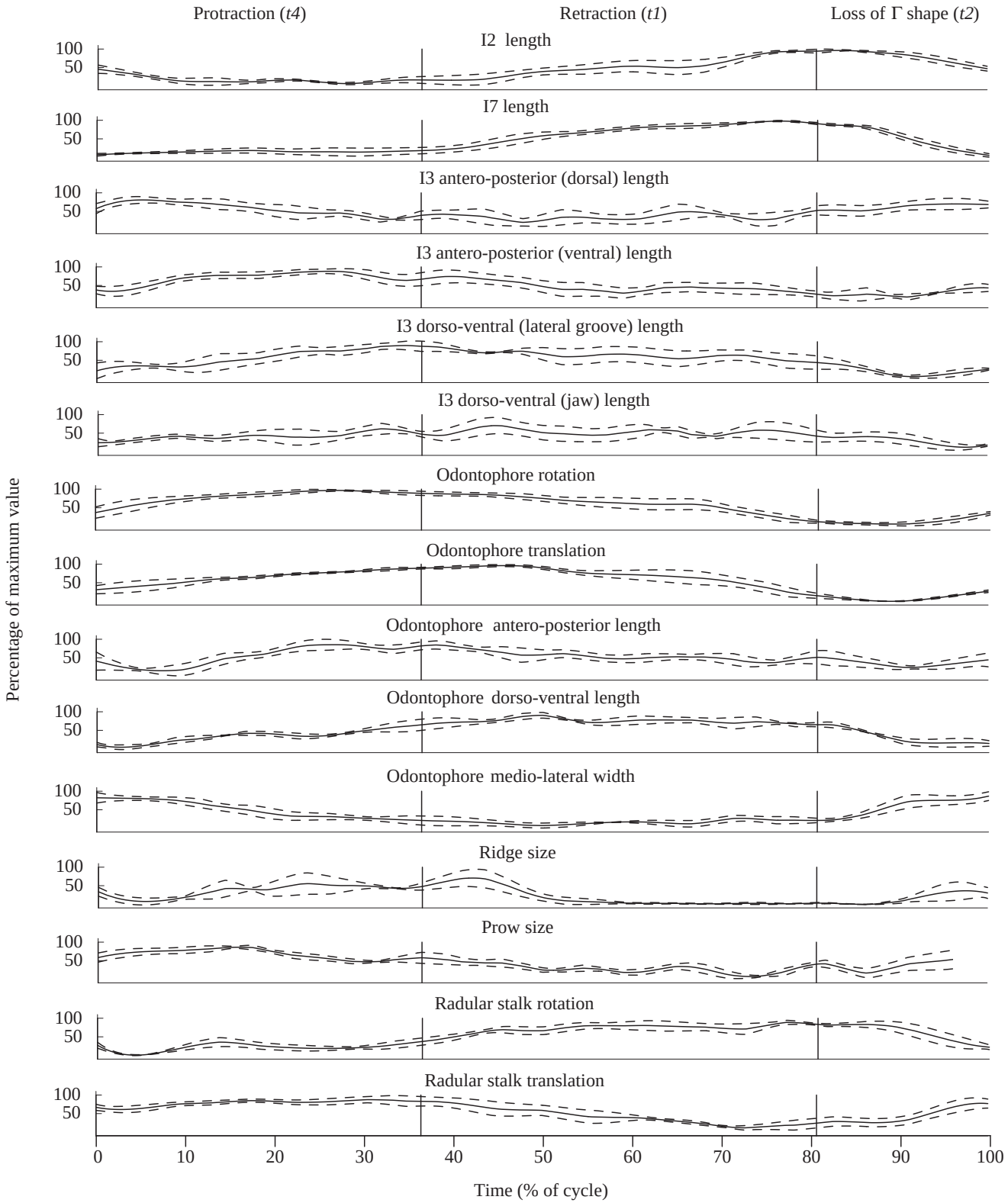

Fig. 18. Averaged kinematics of a single swallow based on the data presented in Neustadter et al. (2002) and the present paper. Averaged values (as a percentage of the maximum value), based on all four swallows, are shown as a solid line; dashed lines show ±1 S.D. (N=4). Data for I2, I3, odontophore rotation and translation, odontophore antero-posterior and dorso-ventral length and radular stalk rotation and translation are all based on direct measurements from the MRIs; see Neustadter et al. (2002) for details. Data for I7, odontophore medio-lateral width, ridge size and prow size are based on predictions of the kinematic model described in this paper. The *y*-axis indicates 100% and 50% of the excursion from the minimum to the maximum value of the variable indicated over each individual graph *versus* normalized cycle time. See Discussion for a detailed analysis.

inaccurate. However, as the odontophore protracts with its halves open into the I3 jaw musculature, the cleft is likely to be large (e.g. Fig. 1A, top view), and this limitation of the model is likely to be most significant. We approximated the size of this error by measuring the area of the cleft at its widest extent from a top view of the isolated odontophore and divided this area by the area of the top view of the entire odontophore. The resulting value was 8.5%, which is an overestimate of the cleft volume, since the cleft does not extend completely from the dorsal to the ventral surface of the odontophore. Since our symmetric difference error is approximately 13%, we believe that any errors introduced by the absence of the cleft volume would not be distinguishable because of the size of the measurement error.

A final limitation of the current model is its inability to provide detailed kinematic descriptions of many of the individual muscles of the odontophore. A full kinematic description of the buccal mass will require an improved inside-out model that explicitly represents the radular surface and the I4, I5 and I6 muscles. With an explicit representation of the I4 muscles and the base of the radular stalk, it will also be possible to describe the kinematics of the I7, I8, I9 and I10 muscles (Evans et al., 1996) and of the leaflets of the I4 muscles that insert medially onto the radular stalk (Evans and Cropper, 1998). The constraints provided by the current model of the kinematics of the odontophore will be essential for defining the kinematics of these muscles.

Comparison with previous models

To understand the kinematics of the buccal mass, we have created a series of increasingly complex models. By starting with simplified models and by carefully comparing these models with biological data, it has been possible to pinpoint those aspects of the models that corresponded accurately to the biological system and to identify the assumptions and properties of the models that caused them to fail to match the biological data.

Assuming that the radula/odontophore could be represented as a rigid sphere generated a reasonable approximation to the shape of the buccal mass near the peak of protraction, but failed to capture the overall shape of the buccal mass during the remainder of the swallowing cycle (Drushel et al., 1998). Assuming that the radula/odontophore could be represented by fixed radula/odontophore shapes obtained by passively deforming it into protraction-like or retraction-like shapes provided a better match to the shape of the buccal mass in specific parts of the feeding cycle, but did not provide a continuous model of the shape of the buccal mass throughout swallowing (Drushel et al., 1998). Assuming that the mid-sagittal shape of the modeled odontophore should be constrained by the shape observed in mid-sagittal MRIs and that the full range of shapes could be generated by rotating or pitching the halves of a rigid-body radula relative to the radular stalk generated a continuously changing odontophore shape that was convincing in mid-sagittal view, but was excessively wide medio-laterally when the radular halves were open (Drushel et al., 2002). Assuming that the odontophore was a smooth, globally convex shape (also constrained by the shapes observed in mid-sagittal MRI), that its maximal medio-lateral width corresponded to a line connecting the extremes of the mid-sagittal cross section and that the ventral base of the radular stalk corresponded to the ventral base of the mid-sagittal odontophore shape generated better overall mid-sagittal shapes for the buccal mass, but was still inaccurate medio-laterally (Drushel et al., 2002). Thus, each model provided guidance for the development of an improved successor model and at the same time generated specific, testable hypotheses for different aspects of the function of the radula/odontophore.

The major differences between the model described in this paper and a previous odontophore-centric model (Drushel et al., 2002) are the kinematically determined angle of the line of widest medio-lateral extent (fixed in the previous model), the inclusion of the ridge and the prow (absent in the previous model) and the ability of the current model to separate the base of the radular stalk from the base of the odontophore (assumed to be the same in the previous model). To test the importance of each of these components, we performed 'lesion' studies on the current model in which each of the new features was removed. A fixed line of widest extent was used at the average value observed, which was a line perpendicular to the vertical prow line. The symmetric difference between the resulting coronal images and the MR coronal images averaged 13%. Similarly, we ran the model without constructing the ridge and found that the symmetric differences averaged 13%. We also removed the prow and found that the symmetric difference averaged 12%. Finally, we placed model odontophores created by the previous odontophore-centric model within the modified I3 model using polynomial limit lines rather than straight lines. Although the mid-sagittal fits were good, there were very large discrepancies in the coronal fits (41%). These results suggest that the most important of the changes made from the previous model was separating the base of the radular stalk from the base of the odontophore. An improved model of the I3 musculature would be likely to respond much more accurately to the relatively small differences in the odontophore shape due to the changing angle of the line of widest extent, to the prow and to the ridge. Even if these features have little effect on the overall fit, they are clearly important for making inferences about the internal kinematics of the radula/odontophore.

Functional implications of the model for the buccal mass

At the outset, it is important to emphasize that a kinematic model can provide only correlative information about the relative positions of system components, not causal statements about the function of the system, since it does not incorporate forces. However, preliminary work on a simplified kinetic model suggests that inferences about muscle function based on a simpler kinematic model were in fact valid (Chiel et al., 2000; G. Sutton and H. J. Chiel, unpublished observations), and hypotheses based on kinematics are therefore a useful starting point for understanding function.

Functional implications of the prow

A significant improvement of the current kinematic model is that the rate of change in the width of the I3 muscle is similar to that observed in the *in vivo* data, unlike the previous kinematic models in which the widths of the I3 muscle changed abruptly (Fig. 15; compare figs 8, 10 and 12 in Drushel et al., 2002). Although the model cannot directly demonstrate the function of the prow, the kinematics observed in the MRIs and in the model suggest two functional roles for the prow. (i) The wedge-like shape of the prow and its position relative to the most posterior I3 ring at the onset of protraction suggest that it may serve to separate the apposed halves of the I3 jaw musculature as the odontophore begins to protract through the jaw musculature's narrow lumen, allowing opening to occur less abruptly. (ii) By increasing the arc-length of the anterior edge of the odontophore, the prow may increase the amount of translation for a given rotation (this is observed for a simple physical model of the odontophore with and without the prow; D. M. Neustadter, unpublished observations). In turn, an increase in translation for a given amount of rotation may improve the efficiency of biting, swallowing and rejection.

Functional implications of muscle kinematics

Functional inferences about muscles I2, I7 and I4 can be drawn from the data. The overall kinematics of the I2 muscle is similar to that described by direct measurements from the MRIs (Neustadter et al., 2002). The I7 muscle lengthens by an average of 165±32% (mean ± S.D., N=4) relative to its minimum length during the four swallows (range 203–124%). This predicted length change is less than that predicted by the previous odontophore-centric model (Drushel et al., 2002) and is within the physiological range of the muscle (Evans et al., 1996). The kinematics of each of the two I4 muscles, lima-bean-shaped muscles that occupy much of the volume of the odontophore and that are connected anteriorly by the I6 muscle, can be inferred from the antero-posterior and dorso-ventral lengths of the whole odontophore (Neustadter et al., 2002) and half the medio-lateral width of the odontophore predicted by the model (Figs 17, 18). During the protraction phase, I4 appears to lengthen both dorso-ventrally and antero-posteriorly as it contracts medio-laterally, corresponding to the open radula being compressed as it protracts through the I1/I3/jaw musculature. During retraction, I4 remains contracted medio-laterally, lengthens dorso-ventrally and contracts in its antero-posterior dimension, which may correspond to a strong radular closure during retraction. During the loss of the Γ shape, I4 lengthens medio-laterally and contracts very significantly dorso-ventrally and to a lesser extent antero-posteriorly, corresponding to the opening of the radular halves.

Radular opening prior to protraction, and the I2 muscle

A striking feature of swallowing is the rapid reduction in the dorso-ventral height of the odontophore after the peak of retraction. We first noted this phenomenon in transilluminated animals and termed it 'the loss of the Γ shape' (Drushel et al., 1997). The mid-sagittal MRIs clearly showed that the dorso-ventral shortening of the odontophore occurred as a result of the movement of the radular stalk into the odontophore (see Fig. 13, right traces, *t2* period, in Neustadter et al., 2002). As the dorso-ventral height of the odontophore rapidly decreases, its medio-lateral width rapidly increases (see fig. 12, right traces, *t2* period, in Neustadter et al., 2002) (see also Figs 17, 18). In two of the four swallows, we also noted that the I2 muscle did not begin to shorten significantly until after the medio-lateral width of the odontophore had rapidly increased (see fig. 7C,D, *t2* period, in Neustadter et al., 2002) (see also Fig. 17C,D; *t2* period). These observations, together with previous observations that the translation of the radular stalk into the odontophore occurs near the end of retraction (see fig. 13, right panels, *t1/t2* transition in Neustadter et al., 2002) and the timing of I2 activation, suggest that the change in the shape of the odontophore after the peak of retraction is not due to an active I2 contraction. Rather, it appears that forces internal to the odontophore, e.g. the contraction of the I7 muscle, cause a rapid upward movement of the stalk that pushes apart the two I4 muscles and opens the radular halves prior to their protraction through the lumen of the I3 musculature. This is consistent with *in vitro* observations of the function of I7 (Evans et al., 1996). During swallowing, active contraction of I2 may be primarily responsible for the initial protraction of the opened radula/odontophore.

A context-dependent role for the radular stalk in opening and closing

The observations of the changing position of the radular stalk within the odontophore near the peak of retraction suggest that it plays a major role in opening the radular halves. Other observations, however, suggest that, in a different mechanical context, the positioning of the radular stalk may also play a major role during radular closure (Fig. 19). Near the peak of protraction, we observed that the stalk remains between the two I4 muscles at the same time that the ridge protrudes significantly dorsally (Figs 8C, 19B), at which time the odontophore both increases in height dorso-ventrally and decreases in width medio-laterally. Only after these changes have occurred does the stalk move downwards and protrude out of the odontophore (Fig. 19C). Although the model does not represent the radular cleft, which defines the inner borders of the I4 muscles, it is possible to infer the likely locations of the I4 muscles using the borders of the radular stalk and the radular ridge. These suggest that the radular stalk may be held firmly between the two I4 muscles so that, when they contract, they will expand upwards and pinch together, allowing the radula to grasp material somewhat further out than it could have if the radular stalk immediately moved downwards as the I4 muscles contracted (Fig. 19B). Thus, the kinematics of the odontophore suggest that, in the mechanical context of protraction, the radular stalk may contribute significantly to the process of radular closing.

Muscle activations and functions throughout the swallowing cycle

It is possible to relate the kinematics that we have observed

to the activity of specific nerves and muscles within the buccal mass. Previous studies have recorded the activity on the major nerves and muscles of the buccal mass in intact, behaving animals during swallowing responses and in isolated buccal masses during swallowing-like movements. In particular, *in vivo* recordings of large extracellular units from buccal nerve 2 (which primarily innervates the I1/I3/jaw musculature) and the radular nerve (which primarily innervates the I4 muscles) have been used to distinguish ingestion-like and rejection-like behaviors (Morton and Chiel, 1993a), *in vivo* recordings from the I2 muscle have been used to examine the role of I2 during protraction in biting, swallowing and rejection (Hurwitz et al., 1996), recordings from the I5 (ARC) muscle during a bite/swallow have been published as part of the study of the modulation of this muscle by peptidergic co-transmitters released by its motor neurons, B15 and B16 (Cropper et al., 1990a,b) and recordings from the I10 muscle (which are thought to be representative of activity in I7, I8 and I9) in intact animals have been published during biting and swallowing behaviors (Evans et al., 1996). Additional data on nerve and muscle activity have been obtained from semi-intact preparations capable of generating feeding-like motor patterns (Morton and Chiel, 1993b; D. W. Morton and H. J. Chiel, unpublished observations). In many cases, these data can be normalized to a single swallowing cycle by using the time from the onset of I2 activity (i.e. the initiation of the protraction phase) to the end of the inward movement of food (i.e. the end of the retraction phase, prior to the initiation of the next protraction phase) or by using the duration of the inward movement of food. These data must be regarded as no more than an initial schematic view until it is possible to obtain simultaneous recordings of nerve and muscle activity during swallowing in intact animals.

We will analyze the cycle of swallowing from the initiation of protraction through the return to the state in which the odontophore has shortened and the radular stalk has moved within the odontophore because this appears to be the sequence in which behaviors are initiated by the feeding pattern generator. Observations of a sequence of swallows using MR imaging indicated that, once protraction had been initiated, a complete cycle of activity was observed. We also observed that pauses between successive responses occurred after the dorso-ventral shortening of the odontophore and the upward movement of the radular stalk into the odontophore, and that the buccal mass would pause for variable amounts of time before initiating another swallow. This observation is consistent with our previous work showing that the initiation of all feeding responses begins with protraction, because the interneurons that initiate activity in the pattern generator, B31/B32, are also motor neurons for the I2 muscle (Hurwitz et al., 1996).

Phase 1: initiation of protraction. Activity in the I2 muscle and on buccal nerve 1 (BN1) is observed at the onset of protraction (Fig. 20). The I2 muscle shortens during the initial phase of protraction (Fig. 18, I2 length in *t4* period). Since BN1 innervates the pharyngeal tissue posterior to the lateral groove and dorsal to the I2 muscle, simultaneous activity of BN1 and the I2 muscle may represent activation of motor neurons that induce all the tissue posterior to the lateral groove to contract, pushing the radula/odontophore anteriorly towards the jaws (Fig. 21, columns 1–3). At the same time, activity is observed on buccal nerve 3 (BN3). Since motor neurons that travel *via* BN3 innervate the 'hinge' tissue, the interdigitation of ventral I4 fibers with the ventral posterior fibers of the I3 muscle (H. J. Chiel, unpublished observations), the activity on BN3 could represent motor neurons that cause contraction of the hinge tissue, inducing an anterior rotation of the radula/odontophore (Fig. 18, odontophore rotation in *t4* period; Fig. 21B, columns 1–3). Note that the odontophore continues to translate and rotate anteriorly even after the I2 muscle has ceased to contract further (Fig. 18, *t4* period).

Shortly after the onset of activity in the I2 muscle, a burst is observed in the I7 muscle. This could be responsible for the shortening observed in I7 during the protraction phase (Fig. 16, *t4* period). In turn, this could have two effects. First, during protraction, the odontophore is pushed through the lumen of the jaws and, using the stalk to separate the two I4 muscles, may aid in keeping the radula open as it is compressed by the surrounding I1/I3/jaw musculature. Second, when the two I4 muscles begin to contract together medially, the presence of the radular stalk may force them to deform dorsally into a ridge. Thus, I7 may participate during the closure of the radular halves (Fig. 19B,E).

During the early phase of protraction, small units are active on buccal nerve 2 (BN2) at a low frequency. It is possible that this could reflect the activity of jaw opener motor neurons (Church and Lloyd, 1994) that could help relax the jaw musculature as the radula/odontophore protracts through it. It could also reflect activity of motor neurons innervating I1, which could act to shorten the dorsal surface of the jaw musculature significantly and aid protraction (note the antero-posterior shortening of I3 on the dorsal surface during the protraction phase; Fig. 18; *t4* period).

Phase 2: protraction/retraction border. After a gap in activity near the end of protraction, BN2 becomes active again, and these units represent motor neurons (e.g. B10) that innervate the I1/I3/jaw musculature and induce contractions (Morton and Chiel, 1993a,b). This corresponds to the time at which the odontophore stops rotating towards the jaw and begins rotating away from the jaws (Fig. 18, odontophore rotation at *t4/t1* border; Fig. 21B, columns 3 and 4), suggesting that compression of the odontophore by the I1/I3/jaw musculature acts to initiate retraction. The cessation of activity in I2 and BN1 should also cause the tissue posterior to the lateral groove to relax, so that it will not resist as the odontophore retracts into the I2 muscle and pharyngeal tissue.

At the same time, activity is observed in large units on the radular nerve, and these units represent motor neurons (e.g. B8a and B8b) that innervate the I4 muscles and induce radular closure (Morton and Chiel, 1993a,b). Closure of the radular halves at the protraction/retraction transition is consistent with maximum protrusion of the ridge (Figs 8C, 18, ridge size at

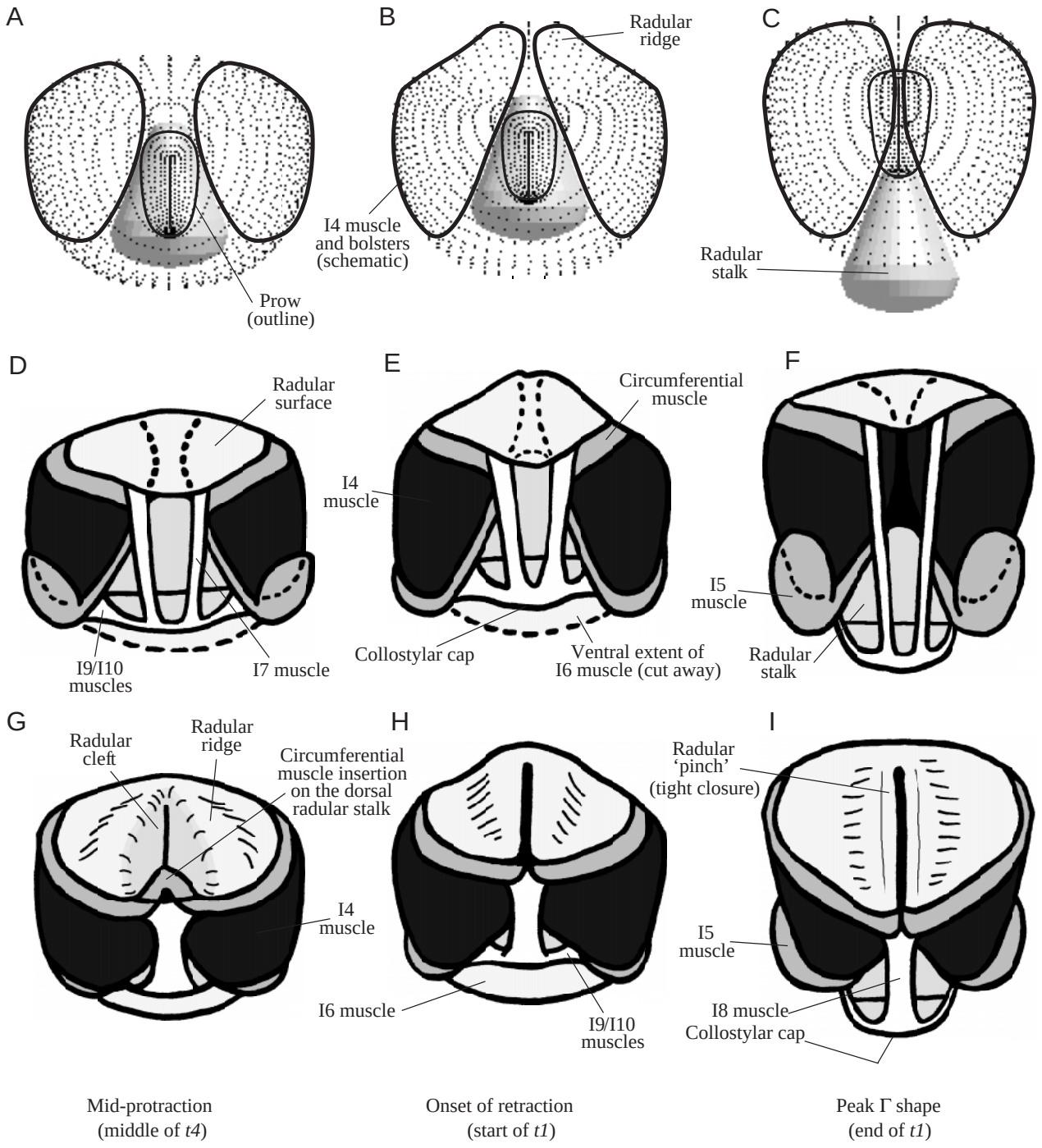

t4/t1 border; Fig. 19B). The radular halves remain closed throughout retraction, pulling food into the buccal cavity.

Activity is observed in large units on BN3 that are likely to represent the activity of the B4/B5 multi-action neurons (Warman and Chiel, 1995). B4/B5 could inhibit the I2 motor neurons (H. Ye and H. J. Chiel, unpublished observations), helping to terminate the protraction phase of swallowing and also to delay the onset of firing of the jaw motor neurons (Gardner, 1977, 1993), allowing the radula/odontophore to move posteriorly so that, when the jaw motor neurons do begin to fire, the I1/I3/jaw muscle complex is positioned anterior to the midline of the odontophore, allowing it to retract the odontophore strongly.

At the onset of the inward movement of food, the I5 (ARC) muscle begins to show electromyographic activity, reflecting activity in the B16 motor neuron (Cropper et al., 1990b). If the radular stalk is between the two I4 muscles (Fig. 19B), and the I4 muscles are stiff as a result of their own activation, contraction of the I5 muscles, which insert both on the lateral margins of the I4 muscles and on the base of the radular stalk, could aid in pulling the radular stalk out of the odontophore. At the same time, compression of the I4 muscles resulting from

Fig. 19. Inferences about the context-dependent function of the radular stalk, I7 and I5 from odontophore kinematics. All illustrations are in orthographic projection, with the radula/odontophore rotated such that the radular stalk is vertical. The top row (A–C) shows transparent antero-posterior views of the model from fully open to just after radular closure. The middle row (D–F) shows antero-posterior views (i.e. through the jaws) of the radula/odontophore with the inferred locations of its constituent muscles indicated schematically. The bottom row (G–I) shows postero-anterior views (i.e. through the esophagus) of the radula/odontophore with the inferred locations of its constituent muscles indicated schematically. The first column shows the radula/odontophore before peak protraction (*t4* period) from frame 22 of sequence 7732-S3. The inferred borders of the I4 muscles are drawn using thick black lines. Note that the radular stalk is entirely within the odontophore (A,D) and that the radula is open (G). The second column shows the radula/odontophore at the onset of retraction (start of *t1*) from frame 26 of sequence 7732-S3. The radular stalk is still entirely within the odontophore. We hypothesize that the presence of the stalk between the I4 muscles as they begin to compress together induces the I4 muscles to deform upwards and form a ridge (B,H), enhancing their ability to grasp food as they close. Note the shortening of the I7 muscles (E) relative to early protraction (D). If the I7 muscles contribute to holding the radular stalk between the I4 muscles, they could enhance the early phase of closing in this configuration. The third column shows the radula/odontophore during retraction (end of *t1* period) from frame 34 of sequence 7732-S3. The radular stalk has moved maximally out of the odontophore, allowing the I4 muscles to close on one another as the radular surface rolls downwards. This induces the formation of the radular 'pinch' (I), and also lengthens the I7 muscles (F), so that their contraction can pull the radular stalk upwards and separate the I4 muscles (i.e. the I7 muscles and the radular stalk can open the radular halves by changing their configuration from column 3 to column 1). Contraction of the I5 muscles can contribute to closing (E) by pulling the radular stalk out of the I4 muscles, and contraction of the I4 muscles can further push the radular stalk downwards, causing the radular halves to close as the odontophore changes from its column 2 to its column 3 configuration. However, relaxation of the I4 muscles and movement of the radular stalk into the odontophore, separating the I4 muscles and lengthening the I5 muscles, could allow a contraction of the I5 muscles to cause the I4 muscles to rotate outwards, so that I5 may enhance opening (changing the odontophore from its column 3 configuration to an open configuration; column 1 shows the odontophore after the peak opening of the radular halves).

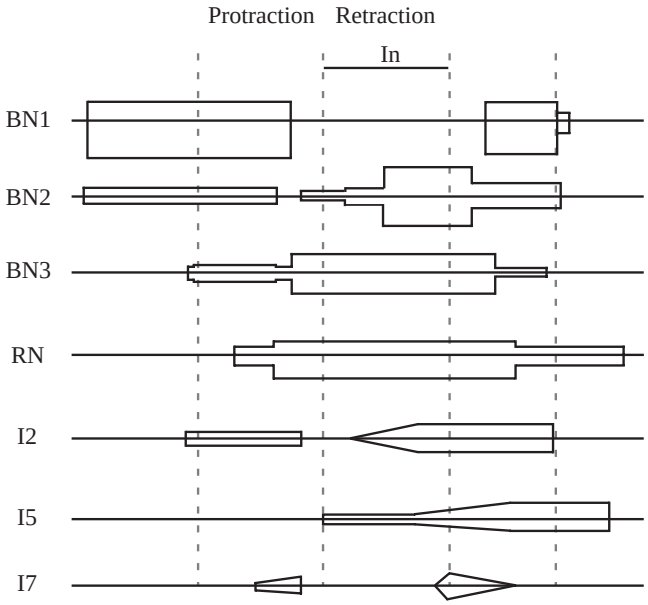

Fig. 20. Schematic representation of neural and muscular activations during a single swallowing cycle. Images of extracellular recordings from nerve and muscle in intact, behaving animals were scanned from several different sources. Simultaneous recording from buccal nerve 2 (BN2) and the radular nerve (RN) were taken from Morton and Chiel (1993a). Simultaneous recordings from BN1, BN2 and BN3 were taken from unpublished observations of D. W. Morton and H. J. Chiel. Simultaneous recordings from muscle I2 and from BN2 were taken from Hurwitz et al. (1996). Extracellular recordings from muscle I5 (ARC) were taken from Cropper et al. (1990b) and were aligned with simultaneous recordings taken from I5, BN2 and RN during *in vitro* ingestive patterns (D. W. Morton and H. J. Chiel, unpublished data). Recordings from I10 (representative of activity in I7, I8, I9 and I10; thus, the schematic is labeled I7 in the figure) were taken from Evans et al. (1996). The lengths of the scanned recordings were scaled relative to one another using the duration of the inward movement of seaweed, the duration of the burst on BN2 or the total duration of the cycle (onset of I2 activity to end of BN2 burst), depending on which features were common between the data sets. The data sets were then aligned by the onset of the inward movement of seaweed. Boxes were then drawn around the resulting extracellular recordings, providing a schematic representation of the relative sizes of the extracellular units and their timing relative to one another.

neural activation and compression of the odontophore by the surrounding I1/I3/jaw musculature could aid in pushing the radular stalk out of the odontophore. The wedge shape of the radular stalk and the smooth, inelastic inner surfaces of the I4 muscles could aid in this process. All these movements induce the radular surface to roll inwards, aiding it in pulling food into the buccal cavity (Fig. 18, radular stalk translation at the *t4/t1* border; Figs 19C,F,I, 21, columns 3–5).

Phase 3: mid-retraction. Midway through retraction, activity is observed in large units on BN2 and facilitating activity is observed on I2. This may correspond to the point at which the elongated odontophore is rotating so that its tip is pushing on the dorsal surface of the I1/I3/jaw musculature (see fig. 5 in Neustadter et al., 2002, frame 16). A burst of activity in BN2 may represent an intensification of closing forces, which cause the rapid retraction ('snap back') that is observed kinematically (Neustadter et al., 2002). At the same time, the late facilitating activity in I2, which may be due to the underlying I4 muscles, may act to brake the rapid retraction (Hurwitz et al., 1996) since I2 is being activated at the same time that it is being stretched. Passive forces in I2 may also act to brake the retraction (Yu et al., 1999).

Phase 4: end of retraction. After food has stopped moving inwards, there is a burst of activity in the I10 muscle (and, presumably, in the I7–I9 muscles; Evans et al., 1996) and the I7 muscle shortens (Fig. 16, *t2* period; Fig. 18, I7 length, *t2*

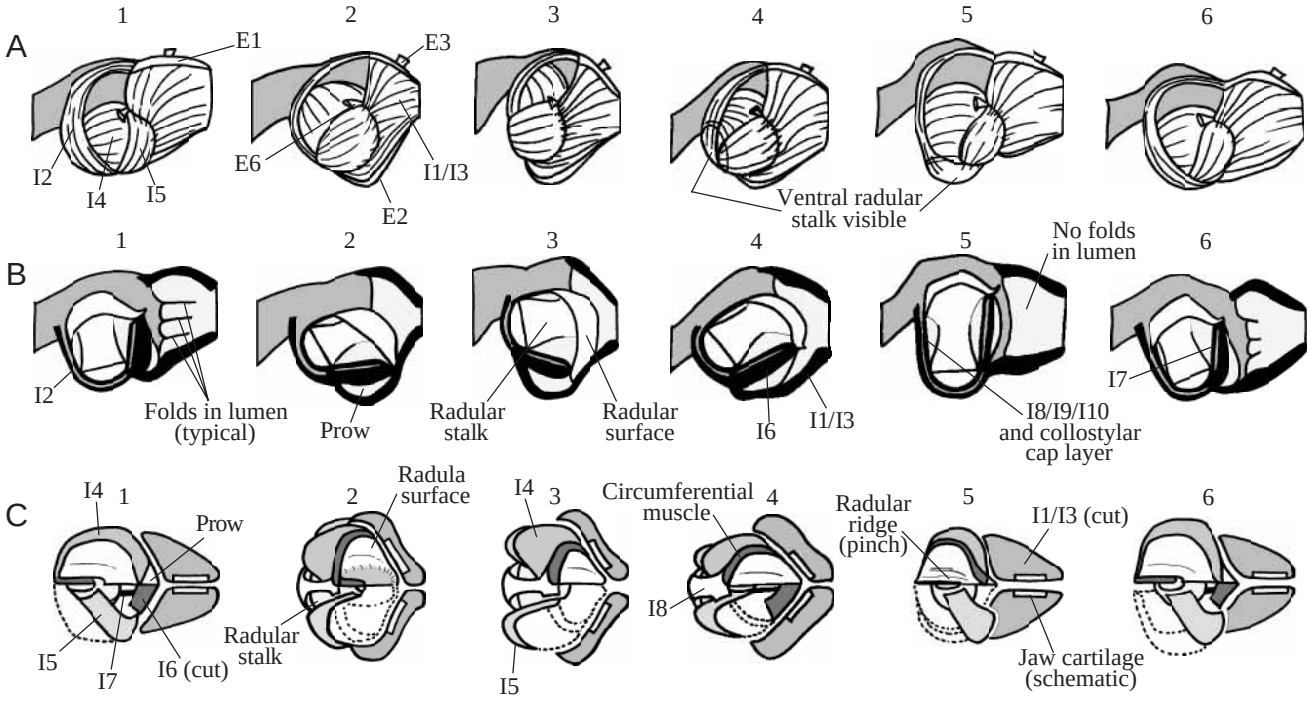

Fig. 21. Schematic summary of the movements of the entire buccal mass during a swallowing cycle. This summary, which supersedes fig. 10 of Drushel et al. (1997), is based on the data presented in the present paper and in Neustadter et al. (2002) and incorporates observations from *in vivo* high-temporal-resolution MRIs taken in intact, behaving animals as well as high-spatial-resolution MRIs of anesthetized buccal masses. Details not visible in the MRIs are based on observations of buccal masses or isolated odontophores undergoing pharmacologically induced feeding-like movements and on dissections of fresh and fixed buccal masses. All illustrations are in orthographic projection. (A) A superficial lateral view of the outer buccal mass. (B) A mid-sagittal view. (C) A dorsal view. In C, the upper half of each diagram depicts a superficial dorsal view, whereas the lower half depicts a view in which the radular surface and the I4 muscles are transparent, showing the ventral structures beneath them. Columns 1–6 correspond to frames 15, 19, 25, 30, 35 and 37, respectively, of sequence 7732-S3. The circumferential muscle shown in C4 was designated as such by Starmühlner (1956). The nomenclature for the other intrinsic muscles follows Howells (1942) and Evans et al. (1996), and the nomenclature for the extrinsic muscles follows Chiel et al. (1986) and Howells (1942).

period; Fig. 21B, columns 5 and 6). Shortening of the I7 muscle could pull the radular stalk into the odontophore, pushing the I4 muscles apart medio-laterally (Fig. 19C,F shows the position of the radular stalk before the I7 muscles contract; Fig. 19A,D shows the position of the radular stalk after the I7 muscles have contracted) and causing the radular halves to open and release food into the esophagus. Interestingly, during this time, it appears that the I5 muscle continues to be active, showing facilitating activity that is likely to be due to the activity of motor neuron B15 (Cropper et al., 1990b). When the radular stalk is held inside the I4 muscles by a strong I7 contraction and the I4 muscles are relaxed, shortening of I5 may aid in separating the I4 muscles, initiating radular opening, and the actions of I5 may also therefore be context-dependent (Fig. 19F shows the position of the I5 muscles at the peak of retraction, when the I4 muscles are lengthened and stiff; Fig. 19D shows the position of the I5 muscles after the I4 muscles have relaxed, although the I4 muscles would be further apart immediately after the loss of the Γ shape). A previous study has shown that the mechanical advantage of I5 may change with the position of the radular halves (Orekhova et al., 2001), but these kinematic observations suggest that the function of the muscle could change.

Once the odontophore has retracted posteriorly and the radular halves have opened and released food into the esophagus, it is interesting to note a burst in BN1. This may be part of the activation of the pharyngeal and esophageal tissue that transports food by peristalsis from the most anterior portion of the esophagus into the gut. Peristaltic movements that transport food into the gut have been observed both in transilluminated juvenile slugs (Drushel et al., 1997) and in high-temporal-resolution mid-sagittal MRIs (D. M. Neustadter and H. J. Chiel, unpublished observations).

Implications for neuromuscular control of movement

As described in the Introduction, several hypotheses have been proposed for the functional mechanisms of the radula and the underlying odontophore. Some investigators have proposed that it might act like a pulley, others have suggested that it might act like a block and tackle (for a review, see Smith, 1988). Our kinematic studies suggest that it may be misleading to use a single mechanical metaphor to describe the operation of the radula/odontophore throughout the entire feeding cycle.

Instead, it appears that small muscles (e.g. I7) act to change the relative positions of larger muscles (e.g. the I4 muscles) and, by doing so, create the appropriate mechanical context for the large muscles to effect a particular behavior (e.g. opening or closing). By shifting among different mechanical contexts, the same set of muscles can flexibly generate a much larger repertoire of behaviors, such as biting, swallowing, rejection, tearing, grazing and cutting (Hurwitz and Susswein, 1992; Kupfermann, 1974; Rosen et al., 2001). The flexible mechanical architecture of this peripheral structure lends itself to a reorganizing neural architecture in which relatively small shifts in the phasing or timing of the activity of different motor pools can generate a range of qualitatively different behaviors (Hurwitz et al., 1997; Jing and Weiss, 2001; Morton and Chiel, 1994).

The work described in this study is likely to contribute to our understanding of neuromuscular control of movement in general. Recent attempts to develop a theoretical understanding of the neuromuscular transform in *Aplysia californica*, the non-linear transformation of neural inputs to motor outputs (Brezina et al., 2000a,b), have incorporated very simple biomechanical constraints (Brezina and Weiss, 2000) and could be greatly improved by incorporating the more realistic relationships between the muscles that are presented in the present paper. Moreover, recent studies of the pattern generator in *Aplysia californica* have shown that it is strongly modulated by proprioceptive feedback (Borovikov et al., 2000; Evans and Cropper, 1998), and the natural kinematics of the musculature is essential for determining the normal proprioceptive feedback that will occur during behavior. Finally, studies of a form of operant conditioning in *Aplysia californica*, in which freely moving animals (Chiel and Susswein, 1993; Susswein et al., 1986) or reduced preparations (Nargeot et al., 1999a,b) can associate specific tastes and textures with inedibility, may be understood within a biomechanical context through the studies described here.

There are more general implications of the studies described in this paper. These studies are an important step towards understanding the interactions between biomechanics and neural control in a muscular hydrostat, i.e. a structure in which muscle may have both force-generating and skeletal functions (Kier and Smith, 1985), and in which forces exerted by the cross section of the muscle as it lengthens or shortens may play important roles. Recent studies of octopus tentacular extension have suggested that, for relatively stereotyped extension movements, a peripheral program within the tentacles may be sufficient (Matzner et al., 2000; Sumbre et al., 2001). Experimental and modeling studies of protrusible tongues and tentacles have also begun to suggest several biomechanical principles for the operation of these structures (van Leeuwen et al., 2000). Studies of the human tongue have suggested that it may have muscular hydrostatic properties during normal speech and swallowing (Nadapow et al., 1999) and that a linear combination of six directions of articular motion involving the tongue, jaw and larynx may sum in a linear fashion to generate speech (Sanguineti et al., 1998). Because of the tractability of the nervous system of *Aplysia californica* to cellular and biophysical analysis, the studies described here may provide the basis for understanding both detailed biomechanics and detailed neural control of a muscular hydrostatic structure. In particular, an understanding of the neural control of context-dependent muscles in *Aplysia californica* may provide insights into the principles of control of context-dependent muscles that have been described in vertebrates. Finally, these studies are serving as the basis for the development of soft-bodied robots whose biomechanics and neural control are based on the biomechanics and neural control of animals such as leeches and slugs (Mangan et al., 2002; Vaidyanathan et al., 2000).

We thank the Whitehall Foundation (grant M97-12 to H.J.C.) and the NSF (grant IBN-9974394 to H.J.C.; IGERT NSF 9972747) for supporting this research. We thank Greg Sutton and Dr Randall Beer for comments on an earlier draft of this manuscript.

References

Alt, H., Fuchs, U., Rote, G. and Weber, G. (1998). Matching convex shapes with respect to the symmetric difference. *Algorithmica* **21**, 89-103.

Borovikov, D., Evans, C. G., Jing, J. A., Rosen, S. C. and Cropper, E. C. (2000). A proprioceptive role for an exteroceptive mechanoafferent neuron in *Aplysia*. *J. Neurosci.* **20**, 1990-2002.

Brezina, V., Orekhova, I. V. and Weiss, K. R. (2000a). The neuromuscular transform: The dynamic, nonlinear link between motor neuron firing patterns and muscle contraction in rhythmic behaviors. *J. Neurophysiol.* **83**, 207-231.

Brezina, V., Orekhova, I. V. and Weiss, K. R. (2000b). Optimization of rhythmic behaviors by modulation of the neuromuscular transform. *J. Neurophysiol.* **83**, 260-279.

Brezina, V. and Weiss, K. R. (2000). The neuromuscular transform constrains the production of functional rhythmic behaviors. *J. Neurophysiol.* **83**, 232-259.

Brusca, R. C. and Brusca, G. J. (1990). Phylum Mollusca. In *Invertebrates*, pp. 695-769. Sunderland, MA: Sinauer Associates Inc.

Carefoot, T. H. (1967). Growth and nutrition of three species of opistobranch molluscs. *Comp. Biochem. Physiol.* **2**, 627-652.

Chiel, H. J., Griner, J. and Beer, R. D. (2000). A kinetic model of the buccal mass of *Aplysia*. *Soc. Neurosci. Abstr.* **26**, 643.7.

Chiel, H. J. and Susswein, A. J. (1993). Learning that food is inedible in freely-behaving *Aplysia californica*. *Behav. Neurosci.* **107**, 327-338.

Chiel, H. J., Weiss, K. R. and Kupfermann, I. (1986). An identified histaminergic neuron modulates feeding motor circuitry in *Aplysia*. *J. Neurosci.* **6**, 2427-2450.

Church, P. J., Cohen, K. P., Scott, M. L. and Kirk, M. D. (1991). Peptidergic motoneurons in the buccal ganglia of *Aplysia californica*: immunocytochemical, morphological, and physiological characterizations. *J. Comp. Physiol. A* **168**, 323-336.

Church, P. J. and Lloyd, P. E. (1994). Activity of multiple identified motor neurons recorded intracellularly during evoked feedinglike motor programs in *Aplysia*. *J. Neurophysiol.* **72**, 1794-1809.

Cropper, E. C., Kupfermann, I. and Weiss, K. R. (1990a). Differential firing patterns of the peptide-containing cholinergic motor neurons B15 and B16 during feeding behavior in *Aplysia*. *Brain Res.* **522**, 176-179.

Cropper, E. C., Price, D., Tenenbaum, R., Kupfermann, I. and Weiss, K. R. (1990b). Release of peptide cotransmitters from a cholinergic motor neuron under physiological conditions. *Proc. Natl. Acad. Sci. USA* **87**, 933-937.

Drushel, R. F., Neustadter, D. M., Hurwitz, I., Crago, P. E. and Chiel, H. J. (1998). Kinematic models of the buccal mass of *Aplysia*. *J. Exp. Biol.* **201**, 1563-1583.

Drushel, R. F., Neustadter, D. M., Shallenberger, L. L., Crago, P. E. and Chiel, H. J. (1997). The kinematics of swallowing in the buccal mass of *Aplysia californica*. *J. Exp. Biol.* **200**, 735-752.

Drushel, R. F., Sutton, G. P., Neustadter, D. M., Mangan, E. V., Adams,

B. W., Crago, P. E. and Chiel, H. J. (2002). Radula-centric and odontophore-centric kinematic models of swallowing in *Aplysia californica*. *J. Exp. Biol.* **205**, 2029-2051.

Eales, N. B. (1921). Aplysia. Liverpool: Liverpool University Press.

Evans, C. G. and Cropper, E. C. (1998). Proprioceptive input to feeding motor programs in *Aplysia*. *J. Neurosci.* **18**, 8016–8031.

Evans, C. G., Rosen, S., Kupfermann, I., Weiss, K. R. and Cropper, E. C. (1996). Characterization of a radula opener neuromuscular system in *Aplysia*. *J. Neurophysiol.* **76**, 1267-1281.

Gardner, D. (1977). Interconnections of identified multiaction interneurons in the buccal ganglia of *Aplysia*. *J. Neurophysiol.* **40**, 349-361.

Gardner, D. (1993). Static determinants of synaptic strength. In *The Neurobiology of Neural Networks* (ed. D. Gardner), pp. 21-70. Cambridge, MA: The MIT Press.

Howells, H. H. (1942). The structure and function of the alimentary canal of *Aplysia punctata*. *Q. J. Microsc. Sci.* **83**, 357-397.

Hurwitz, I., Kupfermann, I. and Susswein, A. J. (1997). Different roles of neurons B63 and B34 that are active during the protraction phase of buccal motor programs in *Aplysia californica*. *J. Neurophysiol.* **75**, 1327-1344.

Hurwitz, I., Neustadter, D., Morton, D. W., Chiel, H. J. and Susswein, A. J. (1996). Activity patterns of the B31/B32 pattern initiators innervating the I2 muscle of the buccal mass during normal feeding movements in *Aplysia californica*. *J. Neurophysiol.* **75**, 1309-1326.

Hurwitz, I. and Susswein, A. (1992). Adaptation of feeding sequences in *Aplysia oculifera* to changes in the load and width of food. *J. Exp. Biol.* **166**, 215-235.

Jing, J. and Weiss, K. R. (2001). Neural mechanisms of motor program switching in *Aplysia*. *J. Neurosci.* **21**, 7349-7362.

Kier, W. M. and Smith, K. K. (1985). Tongues, tentacles, and trunks: The biomechanics of movement in muscular-hydrostats. *Zool. J. Linn. Soc.* **83**, 307-324.

Kupfermann, I. (1974). Feeding behavior in *Aplysia*: A simple system for the study of motivation. *Behav. Biol.* **10**, 1-26.

Mangan, E. V., Kingsley, D. A., Quinn, R. D. and Chiel, H. J. (2002). Development of a peristaltic endoscope. In *Proceedings of the 2002 IEEE International Conference on Robot Automation* (ed. W. R. Hamel and A. A. Maciejewski), pp. 347-352. OMNIPRESS.

Matzner, H., Guttfreund, Y. and Hochner, B. (2000). Neuromuscular system of the flexible arm of the octopus: Physiological characterization. *J. Neurophysiol.* **83**, 1315-1328.

Miller, M. W., Rosen, S. C., Schissel, S. L., Cropper, E. C., Kupfermann, I. and Weiss, K. R. (1994). A population of SCP-containing neurons in the buccal ganglion of *Aplysia* are radula mechanoafferents and receive excitation of central origin. *J. Neurosci.* **14**, 7008-7023.

Morton, D. W. and Chiel, H. J. (1993a). *In vivo* buccal nerve activity that distinguishes ingestion from rejection can be used to predict behavioral transitions in *Aplysia*. *J. Comp. Physiol. A* **172**, 17-32.

Morton, D. W. and Chiel, H. J. (1993b). The timing of activity in motor neurons that produce radula movements distinguishes ingestion from rejection in *Aplysia*. *J. Comp. Physiol. A* **173**, 519-536.

Morton, D. W. and Chiel, H. J. (1994). Neural architectures for adaptive behavior. *Trends Neurosci.* **17**, 413-420.

Nadapow, V. J., Chen, Q., Wedeen, V. J. and Gilbert, R. J. (1999). Intramural mechanics of the human tongue in association with physiological deformation. *J. Biomech.* **32**, 1-12.

Nargeot, R., Baxter, D. A. and Byrne, J. H. (1999a). In vitro analog of operant conditioning in *Aplysia*. I. Contingent reinforcement modifies the functional dynamics of an identified neuron. *J. Neurosci.* **19**, 2247-2260.

Nargeot, R., Baxter, D. A. and Byrne, J. H. (1999b). In vitro analog of operant conditioning in *Aplysia*. II. Modifications of the functional dynamics of an identified neuron contribute to motor pattern selection. *J. Neurosci.* **19**, 2261-2272.

Neustadter, D. M., Drushel, R. F. and Chiel, H. J. (2002). Kinematics of the buccal mass during swallowing based on magnetic resonance imaging in intact, behaving *Aplysia californica*. *J. Exp. Biol.* **205**, 939-958.

Neustadter, D. M., Drushel, R. F., Crago, P. E. and Chiel, H. J. (2001). A 3-dimensional model of the odontophore of *Aplysia* throughout a swallowing cycle. *Soc. Neurosci. Abstr.* **27**, 943.7.

Orekhova, I. V., Jing, J., Brezina, V., DiCaprio, R. A., Weiss, K. R. and Cropper, E. C. (2001). Sonometric measurements of motor-neuron-evoked movements of an internal feeding structure (the radula) in *Aplysia*. *J. Neurophysiol.* **86**, 1057-1061.

Pennings, S. C. (1990). Size-related shifts in herbivory: specialization in the sea hare *Aplysia californica* Cooper. *J. Exp. Mar. Biol. Ecol.* **142**, 43-61.

Press, W. H., Flannery, B. P., Teukolsky, S. A. and Vetterling, W. T. (1988). *Numerical Recipes in C: The Art of Scientific Computing*. Cambridge: Cambridge University Press.

Rosen, S. C., Friedman, A. K. and Kupfermann, I. (2001). Control of grazing and browsing feeding behavior in *Aplysia*. *Soc. Neurosci. Abstr.* **27**, 306.28.

Rosen, S. C., Miller, M. W., Cropper, E. C. and Kupfermann, I. (2000a). Outputs of radula mechanoafferent neurons in *Aplysia* are modulated by motor neurons, interneurons, and sensory neurons. *J. Neurophysiol.* **83**, 1621-1636.

Rosen, S. C., Miller, M. W., Evans, C. G., Cropper, E. C. and Kupfermann, I. (2000b). Diverse synaptic connections between peptidergic radula mechanoafferent neurons and neurons in the feeding system of *Aplysia*. *J. Neurophysiol.* **83**, 1605-1620.

Rosen, S. C., Weiss, K. R., Cohen, J. L. and Kupfermann, I. (1982). Interganglionic cerebral-buccal mechanoafferents of *Aplysia*: Receptive fields and synaptic connections to different classes of neurons involved in feeding behavior. *J. Neurophysiol.* **48**, 271-288.

Rosen, S. C., Weiss, K. R. and Kupfermann, I. (1979). Response properties and synaptic connections of mechanoafferent neurons in cerebral ganglion of *Aplysia*. *J. Neurophysiol.* **42**, 954-974.

Sanguineti, V., Laboissiere, R. and Ostry, D. J. (1998). Dynamic biomechanical model for neural control of speech production. *J. Acoust. Soc. Am.* **103**, 1615-1627.

Smith, D. A. (1988). Radular kinetics during grazing in *Helisoma trivolvis* (Gastropoda: Pulmonata). *J. Exp. Biol.* **136**, 89-102.

Sokal, R. R. and Rohlf, F. J. (1981). *Biometry*. San Francisco: W. H. Freeman & Co.

Starmühlner, F. (1956). Beiträge zur Mikroanatomie und Histologie des Darmkanals einiger Opisthobranchier. I. *Sitzungsberichte Mathem-Naturw. Kl., Abt. I* **165**, 8-52.

Sumbre, G., Guttfreund, Y., Fiorito, G., Flash, T. and Hochner, B. (2001). Control of octopus arm extension by a peripheral motor program. *Science* **293**, 1845-1848.

Susswein, A. J., Rosen, S. C., Gapon, S. and Kupfermann, I. (1996). Characterization of buccal motor programs elicited by a cholinergic agonist applied to the cerebral ganglion of *Aplysia californica*. *J. Comp. Physiol. A* **179**, 509-524.

Susswein, A. J., Schwarz, M. and Feldman, E. (1986). Learned changes of feeding behavior in *Aplysia* in response to edible and inedible foods. *J. Neurosci.* **6**, 1513-1527.

Vaidyanathan, R., Chiel, H. J. and Quinn, R. D. (2000). A hydrostatic robot for marine applications. *Robot Auton. Syst.* **30**, 103-113.

van Leeuwen, J. L., De Groot, J. H. and Kier, W. M. (2000). Evolutionary mechanics of protrusible tentacles and tongues. *Neth. J. Zool.* **50**, 113-139.

Warman, E. N. and Chiel, H. J. (1995). A new technique for chronic single unit extracellular recording in freely behaving animals using pipette electrodes. *J. Neurosci. Meth.* **57**, 161-169.

Yu, S.-Y., Crago, P. E. and Chiel, H. J. (1999). Biomechanical properties and a kinetic simulation model of the smooth muscle I2 in the buccal mass of *Aplysia*. *Biol. Cyber.* **81**, 505-513.